Youness *et al. Genome Medicine* (2025) 17:155
https://doi.org/10.1186/s13073-025-01580-z

Genome Medicine

RESEARCH Open Access

Location and aetiology are determinants of fibroblast activation and heterogeneity in the failing human heart

Mohamad Youness[1], Samaneh Ekhteraei-Tousi[1,5], Chandan Kadur Nagaraju[1], Rosa Doñate Puertas[1], Bernard Thienpont[3,4], Filip Rega[2], Karin R. Sipido[1*†] and H. Llewelyn Roderick[1,4*†]

Abstract

Background Cardiac fibrosis is a key feature of pathological cardiac remodelling that significantly impacts heart function through contributing to stiffness, diastolic dysfunction, and arrhythmias, ultimately leading to heart failure (HF). Despite extensive research into fibrosis-related matrix alterations, therapeutic advancements are limited, in part owing to the different nature (reparative vs interstitial) and tissue distribution of fibrosis involved. To identify unique features of fibrosis phenotypes, we investigated fibroblast (FB) heterogeneity and spatial distribution in left ventricular myocardium in HF patients with ischemic (ICM) and dilated cardiomyopathy (DCM). Infarct scar was also analysed.

Methods We performed single-nucleus RNA sequencing of 20 human left ventricular tissue samples: from non-failing, NF ($N=4$), DCM ($N=6$) and ICM ($N=5$) hearts, and from the ICM scar region ($N=5$). The data was subjected to bioinformatic analysis, included clustering, differential expression, ligand-receptor inference, and pseudotime trajectory mapping to delineate FB transitions and regional fibrosis signatures. To identify localisations of FB states and cellular neighbourhoods, data was integrated with publicly available spatial transcriptomics datasets.

Results We identified distinct FB subpopulations across failing and non-failing hearts. Resident FB states showed preferential perivascular and interstitial distribution in NF and exhibited significant depletion in HF, giving rise to different disease states. We identified shared and unique activation ligands driving the onset of FB transitions as well as transcriptional differences between scar and interstitial fibrosis, and between ICM and DCM interstitial fibrosis. Trajectory analysis revealed distinct differentiation pathways for FB depending on its originating resident FB, with specific transcription factors guiding each transition.

Conclusions These findings provide a comprehensive framework for understanding fibroblast dynamics, highlighting the heterogeneity and spatial complexity of fibrosis in human end-stage HF, and offering potential therapeutic targets to mitigate fibrosis while preserving scar integrity.

†Karin R. Sipido and H. Llewelyn Roderick contributed equally as senior authors.

*Correspondence:
Karin R. Sipido
karin.sipido@kuleuven.be
H. Llewelyn Roderick
llewelyn.roderick@kuleuven.be

Full list of author information is available at the end of the article

Keywords Heart failure, Fibrosis, Fibroblast, SnRNA sequencing, Transcriptomics

Background

Cardiac fibrosis remains one of the least tractable features of pathological cardiac remodelling [1, 2], yet it has a major functional impact as fibrosis contributes to stiffening of the heart and diastolic dysfunction, as well as to disturbed electrical conduction and associated arrhythmias. Progressive interstitial fibrosis underlies transition to heart failure (HF) in hypertensive heart disease and contributes to HF with preserved ejection fraction (HFpEF) [3, 4]. Reparative fibrosis occurs subsequent to myocardial infarction (MI), where it serves to maintain cardiac integrity after the loss of cardiomyocytes (CM). Understanding the mechanisms that determine the type of fibrosis induced – beneficial or not—is therefore a priority for the development of new therapies. The well-known beneficial action of angiotensin and aldosterone pathway antagonists against fibrosis [5–8] is partly mediated via effects on the differentiation of fibroblasts (FB) into myofibroblasts (myoFB), the effector cells of matrix remodelling and fibrosis. Inducing de-differentiation of myoFB to a more resting state to reverse fibrosis is an active area of research [9–12]. Pirfenidone, first used for pulmonary fibrosis has now also shown benefit in HF [13]. While the mechanism of action of this drug is not fully established, reducing pro-fibrotic pathways such as TGF-β activation are proposed.

FB phenotypic alterations are induced by different cues, including mechanical load and inflammation [14]. Recent studies have demonstrated how exploiting inflammatory signalling could reduce fibrosis. For example, by immuno-depletion of IL-1β, which is expressed by monocytes and macrophages [15, 16] or engineering T-cells or macrophages to express chimeric receptors against the fibroblast associated protein (FAP) antigen [17, 18]. Furthermore, interaction between CM and FB through paracrine signalling is an essential element in pathological remodelling during pressure overload [19]. These mechanical and/or inflammatory signals, including TGF-β and IL1β, act on FB to increase their capacity to deposit and remodel the ECM, to promote their proliferation, and to adopt a more contractile MyoFB phenotype. While different sources for FB have been invoked such as from endothelial, hematopoietic, or smooth muscle origins, lineage tracing shows that FB achieve these additional functions and phenotypes via differentiation from resident cardiac quiescent FB [20–22].

Single cell RNA sequencing (scRNA-Seq) approaches has accelerated the definitive identification of the diversity of FB phenotypes that explain the different functions described for these cells in the normal and failing heart. These studies have also provided insights into the signalling cues and intercellular signalling pathways activated during remodelling, such as after ischemic injury [23] or angiotensin II stimulation [24]. Further studies analysing intercellular communication and using spatial transcriptomics have led to the concept of cardiac niches with FB subpopulations in nexus with different immune cell types, e.g. CCR2 + macrophages and CM (reviewed in [25]).

Single-nucleus (sn)RNA-seq approaches have also provided new information on the cellular landscape, including that of FB, of the non-diseased human heart [26, 27] and how it is altered in HF, including with dilated cardiomyopathy (DCM) [28–30] and post-MI [31]. Despite this progress, human data on FB biology remain limited, particularly spanning different aetiologies and disease stages. Previously, we identified different FB subpopulations in end-stage human HF, which also suggested differences between DCM and ischemic cardiomyopathy (ICM) but lacked the molecular detail to define these FB states [11]. While recent sequencing efforts have advanced these findings, the nature of the different FB states and their relationships to one another are yet to be fully explored across different aetiologies and locations. Moreover, an understanding of the spatial heterogeneity of resident FB and the local signalling cues that govern their activation states, for example in response to MI, that is required for future targeting, is missing. Indeed, this knowledge is essential for targeting the interstitial and patchy fibrosis that contributes to cardiac dysfunction and arrhythmia while preserving the reparative fibrosis of the infarct scar [32, 33].

In the present study, we therefore investigated whether different aetiologies underlying advanced HF in humans lead to distinct FB signatures, and whether location within the failing heart defined FB phenotypes. In particular, we compared scar tissue to interstitial fibrosis, asking whether unique signatures would allow targeting of these locations independently.

To these ends, we performed deep snRNA-seq of patient samples of NF, DCM, ICM mid myocardium, and ICM-scar. Analysis of the FB identified 9 FB cell states across aetiologies, with some being highly enriched or specific to pathology. These FB states showed distinct patterns of gene expression and potential for regulation by specific ligands. Through integration with a publicly available spatial transcriptomic dataset, FB states were assigned to interstitial, adventitial/vascular, and scar regions of the heart. This analysis revealed the plasticity of cardiac FB and identified local drivers underlying FB heterogeneity in HF thus providing new avenues for their selective targeting.

Methods

Human cardiac tissue

Left ventricular (LV) myocardial tissue samples were obtained from explanted hearts at the time of heart transplantation and from non-used donor hearts, in collaboration with the Transplant team and the Department of Cardiac Surgery, UZ Leuven. Non-failing samples are from donor hearts not used for transplantation, where age allowed valve donation but not transplantation. For all samples, we obtained basic clinical parameters at the time of tissue sampling (cardiac history and functional status, medication, anthropometrics, laboratory measurements). The study protocol conformed to the Helsinki declaration and was conducted according to national and European Union regulations on the use of human tissues and was approved by the ethical committee of UZ Leuven (S58824). Tissue samples were collected under RNase free conditions and immediately snap frozen in liquid nitrogen and stored at – 80 °C for later use.

Tissue sampling

All hearts are stored and transported on ice at all times until freezing for no more than 2 h after removal. All hearts were sampled according to a standardized protocol, where biopsies of midmyocardium for available cardiac regions are directly snap frozen in liquid nitrogen and adjacent transmural tissues are embedded in OCT for immunofluorescence and fibrosis studies. Of particular note, the ICM-scar tissue analysed is taken from heart with a historical MI > 12 months (1–12 years), in which the scar has matured to support the integrity of the heart.

Sample preparation for snRNA-seq

Isolation of high quality intact nuclei from snap frozen cardiac tissue was performed according to our recent study [34]. This protocol is built on expertise in the isolation of CM nuclei from frozen tissue developed in [35] and further optimization based on [36]. In brief, 70–100 mg of Snap frozen mid-myocardium tissues samples were mechanically homogenized using Miltenyi gentleMACS™ Tissue Dissociator with gentleMACS M tubes using the protocol "protein_01" in 5 ml lysis buffer solution (5 mM $CaCL_2$, 3 mM MgAc, 2 mM EDTA, 0.5 mM EGTA, 10 mM Tris–HCL in water supplemented prior to use with 1 mM DDT (Sigma-Aldrich, 646,563), 1 µg/mL actinomycin D (Sigma-Aldrich, A1410), 0.05% protease inhibitor cocktail (Sigma-Aldrich, P8340), and 0.04 U/µL RNA inhibitors-RNase OUT (Thermofisher Scientific, 10,777,019), then incubated on ice for 15 min with extra 5 ml of the same solution supplemented with 0.1% NP-40. The lysate was then gently filtered through a 30 µm filter into a 15 ml conical tube, followed by rinsing the filter once with 2 ml lysis buffer supplemented with 0.1% NP-40. Nuclei were then centrifuged at 1000 g for 5 min at 4 °C. The nuclear pellet was then resuspended in 2 ml of sucrose buffer solution (1 M sucrose, 3 mM MgAc, and 10 mM Tris–HCl supplemented with 1 mM DDT, 1 µg/mL actinomycin D, 0.05% protease inhibitor cocktail, 0.04 U/µL RNA inhibitors-RNase OUT, and 2 µg/mL WGA (Sigma-Aldrich, L9640), and laid over another 2 ml sucrose solution in a 5 ml canonical tube. Centrifugation was repeated according to the above parameters. The supernatant was then removed, and nuclei resuspended in 400 µl nuclei wash buffer (PBS including 0.04 U/µL RNA inhibitors-RNase OUT, 2 µg/mL WGA, and 750 µg/mL UltraPure™ BSA), and centrifuged at 650 g for 6 min at 4 °C. The wash step was repeated as per the previous but with a centrifugation at 500 g. The sample was then resuspended in staining buffer (wash buffer containing 0.02 mg/mL DAPI), for 10 min in 1.5 ml tube. Nuclei were harvested by centrifugation at 500 g for 6 min. The pellet was then resuspended in 300 µl of PBS, pooled with the duplicate pellet of each sample, and filtered through a 35 µ strainer into FACS tubes. Nuclei were sorted based on size and DAPI positivity into 40 µl PBS containing 0.04 U/µL RNA inhibitors-RNase OUT and 750 µg/mL UltraPure™ BSA using a BD Influx flow cytometer with a 100-µM nozzle, and collected in 1.5 ml tubes.

10x library preparation and alignment

Single sorted nuclei were counted using a LUNA-FL™ Counter (Logos Biosystems) in duplicates, after which nuclei were centrifuged and then resuspended to a target concentration of 1,000 nuclei/µl and loaded on the Chromium Controller (10x Genomics) to achieve a targeted recovery of 6,000–10,000 nuclei per reaction. 3′ gene expression libraries were prepared according to the manufacturer's instructions of the v3 Chromium Single Cell Reagent Kits (10x Genomics). Quality control of cDNA and final libraries was carried out by Bioanalyzer High Sensitivity DNA Analysis (Agilent). Libraries were sequenced using a NovaSeq 6000 (Illumina) at the Genomics Core facility at KU Leuven targeting 80,000 read pers nucleus. Nuclei were aligned to the human GRCh38-3.0.0 transcriptome with "Include-introns = TRUE" using the CellRanger (v6.0.1) software (10x Genomics) according to the 10x Genomics instructions.

Background removal with CellBender

All 20 samples were of high quality in terms of number of nuclei, reads per nuclei, and genes detected, and were processed to remove ambient RNA using CellBender [37]. Samples were processed individually using the remove-background tool from CellBender (v0.2.0) to correct gene count matrices by removing ambient background RNA contamination (https://github.com/broadinstitute/CellBender). Default parameters were used except

for expected-cells parameter which was adjusted based on the expected nuclei obtained from CellRanger (v6.0.1) software.

Separating non-HF samples based on sex genes expression

Each HF sample was run on a separate Chromium 10x chip lane. However, non-HF samples were run in pairs and mixed based on sex (one female + one male sample per lane). Sex chromosome genes were used to demultiplex these samples as shown to work previously [38]. CellBender-corrected gene count matrices (HDF5 output files) from each of the two mixed-donor samples were imported into R using the Read10X_h5 function. Donor sex assignment for each nucleus was determined based on expression of Y-chromosome genes, retrieved from the Ensembl reference genome (Ensembl release 108; archived at https://oct2022.archive.ensembl.org). A nucleus was classified as male if the summed expression across all Y-chromosome genes was greater than zero, and as female otherwise.

Removing doublets by scDblFinder

Since the majority of our samples were run individually, there were no homotypic doublets (doublets formed by nuclei of the same cell type) from two different samples. However, heterotypic doublets (doublets formed by nuclei of different cell types), were removed using scDblFinder (v1.16.0) [39] using default parameters. scDblFinder, which uses SingleCellExperiment object (v 1.24.0) with non-stringent filtering of nuclei. Prior to removing doublets, nuclei were filtered for mitochondrial and ribosomal reads < 5%, nCount_RNA > 500, nFeature > 300, and nuclei complexity > 0.8 (estimated by log10(obj$nFeature_RNA)/log10(obj$nCount_RNA)). Thresholding was based on the expected doublet rate which is estimated using the empirical rule applicable to 10 × data, which is approximately 1% per 1000 nuclei captured.

Clustering, sub-clustering, and annotationn of cardiac cell types and FB cell states

Individual sample matrices were imported into the Seurat package (v5.0.1) [40] and combined into a Seurat object after removing background, separating NF samples, and removing doublets. No further filtering was performed on the complete object. Normalization was performed using NormalizeData() function with LogNormalize method and scaling factor of 10,000. Highly variable genes (3000 genes) were obtained by FindVariableFeatures() function using vst method, and scaling was performed using ScaleData() function by regressing mitochondrial reads and nCount_RNA to respect the heterogeneity within the different cell types (CM have higher counts and mitochondrial read % than other cell types). Then, dimensions were reduced by RunPCA(), and samples were integrated using RunHarmony() function (v1.2.0) [41] with default parameters and by considering individual heart source as a batch to account for individual biological heterogeneity. Harmony generated dimensions were used subsequently in the analysis. A nearest-neighbour graph was constructed using FindNeighbors() function using 31 dimensions obtained from elbow plot assessment. The Uniform Manifold Approximation and Projection (UMAP) dimensional reduction technique was performed using the RunUMAP() function with 31 harmony dimensions. Nuclei were clustered with the FindClusters() function, applying the Louvain algorithm at a resolution of 0.2. This resolution was chosen based on prior literature to enable robust identification of the major cardiac cell types. Cluster markers were identified using Wilcoxon tests as implemented in Seurat's FindAllMarkers function with parameters logfc.threshold = 0.5 and min.pct = 0.1, and p values were adjusted using the Bonferroni method. Final assignment of clusters to major cardiac cell types was guided by established marker genes reported in the literature. Annotations were validated using Azimuth's reference-based annotation (v0.4.6) [26, 29, 40, 42] and automated heart mapping with default settings (Additional file 1: Fig. S1g).

FB sub-clustering was performed by subsetting FB nuclei and redoing similar steps as above with the following differences: the number of variable genes was set to 2000 using the vst method, scaling was performed while regressing nCount_RNA only, mitochondrial genes were removed prior to marker analysis, 34 harmony dimensions were used, for creating UMAP and finding neighbours, and 0.4 resolution was used for clustering. The clustering resolution was selected empirically to balance over-splitting with sufficient granularity to resolve biologically meaningful subpopulations, guided by marker genes of clusters at different resolutions, and by assessing clustering trees origins as resolution increases using clustree (v0.5.1) [43]. Additionally, clusters were compared and contextualized with published single-cell cardiac atlases (see below). FB cell states markers were identified using Wilcoxon tests as implemented in Seurat's FindAllMarkers function with parameters logfc.threshold = 0.25 and min.pct = 0.1, and p values were adjusted using the Bonferroni method.

Comparison of FB clusters to literature

To compare our FB clusters with those described in published studies, we applied the Tversky index ($\alpha = 0.5$, $\beta = 0.5$) to quantify similarity between FB states marker gene sets to those from [16, 26, 29, 31, 44, 60, 68, 69]. Index values range from 0 to 1, with higher scores reflecting greater overlap. Similarity scores were computed

against reference clusters from prior cardiac fibroblast atlases and visualized as heatmaps, allowing us to contextualize our clusters relative to known fibroblast states and highlight subtle transcriptional distinctions (Additional file 1: Fig. S5). Similarly, we compared our FB clusters with those reported in atherosclerosis from Wirka et al. [45] using the Tversky index.

Cell type composition analysis

To test for differences in FB cluster composition across disease groups, we used the speckle R package (v 1.2.0) [46]. Cluster proportions were calculated and transformed per sample using getTransformedProps with 'logit' transformation. Differences in overall cluster composition across groups (NF, DCM, ICM, and ICM-scar) were first tested using propeller.anova. Pairwise group comparisons were then performed with propeller.ttest using contrasts defined in a linear model design matrix. Multiple testing correction was performed using the Benjamini–Hochberg false discovery rate (FDR) procedure. Only clusters that were significant in both the global ANOVA (FDR < 0.05) and at least one pairwise test (FDR < 0.05) were retained as robust findings.

SASP module scoring across fibroblast clusters

We computed a senescence-associated secretory phenotype (SASP) module score per nucleus using Seurat AddModuleScore function with a curated SASP gene set [47], then compared scores across FB clusters using violin plots with cluster means overlaid.

Differential gene expression analysis

Differential expression was assessed using a pseudobulk strategy using DESeq2 package (v1.42.0) using default settings unless specified otherwise [48]. Lowly expressed genes were filtered by retaining only those with counts > 1 in at least 10 cells. Pseudobulk counts was modelled with a negative binomial generalized linear model, with median-of-ratios normalization. Significance testing was performed with Wald test. Multiple testing correction was performed using the Benjamini–Hochberg FDR method.

To assess whether specific cardiac cell types exhibited stronger transcriptional responses in each HF condition compared to NF, we compared the number of differentially expressed genes (DEGs) identified in each major cardiac cell type across disease conditions vs NF. For this purpose, single-nucleus profiles were aggregated into pseudobulk counts per cluster and per sample using Seurat::AggregateExpression (sum method). Differential expression analysis was then performed at the sample level with DESeq2. For each cluster separately, a DESeq2 dataset was constructed with design = ~condition (condition levels: NF, DCM, ICM, ICM-scar). Contrasts were defined to compare each disease group against NF (DCM-NF, ICM-NF, ICM-scar-NF). Genes were considered differentially expressed if they met both statistical significance and effect size thresholds: an adjusted p value (Benjamini–Hochberg correction) < 0.05 and an absolute log2 fold-change (|log2FC|) > 1. To control for compositional effects on DEG detection, we downsampled each major cell type in every sample to equal abundance and repeated the analyses, yielding nearly identical results (Additional file 1: Fig. S3d-e).

For the activated FB state comparison, we restricted the analysis to nuclei belonging to FB1 and FB4 clusters. Pseudobulk counts were aggregated per cluster and per sample, and differential expression was tested with DESeq2 using a design formula ~ cluster. A contrast was defined to compare FB4 versus FB1. To specifically investigate extracellular matrix remodeling, we intersected the DEG results with a curated matrisome gene set [49] https://github.com/mahmoudibrahim/KidneyMap. ECM-related DEGs were further filtered by requiring an absolute $\log_2$ fold-change greater than 0.5 and an adjusted p value < 0.05, and were annotated as upregulated in either FB4 or FB1.

To identify transcriptional programs distinguishing resting from activated FB states to identify resting-activated state pairs, we applied the same pseudobulk differential expression strategy as described above. Differential expression was performed separately within the three resting fibroblast clusters (FB0, FB2, FB3) and within the activated fibroblast clusters (FB1, FB4, FB5). For each cluster, one-versus-rest contrasts were defined using a no-intercept design (design = ~0 + cluster) and numeric contrasts to compare each cluster against the other two. Genes were considered significant if they met both statistical and effect size thresholds (adjusted p value < 0.05 and $\log_2$FC > 1, selecting genes upregulated in the focal cluster). The resulting gene sets were then intersected to identify commonly regulated genes across resting and activated fibroblast states, enabling the definition of "resting–activated pairs." Overlap between these gene sets was visualized using the UpSetR package (v 1.4.0) [50].

In addition, direct comparison of ICM vs DCM FB was performed at the single-nuclei level using Seurat's Wilcoxon rank-sum test (FindMarkers) with thresholds of |avg_log2FC| > 0.25 and adjusted p value < 0.05. To further distinguish aetiology-specific differences from those associated with fibrosis, we repeated this comparison in a pseudobulk framework while explicitly modeling fibrosis. Counts were aggregated per sample, and a DESeq2 model was fitted with the design ~ condition + fibrosis_z, where fibrosis was standardized (z-scored) per sample. This allowed testing of DCM vs ICM differences while adjusting for fibrosis burden as a continuous covariate,

to ensure that identified signatures were independent of fibrosis levels.

Pathway analysis by ClusterProfiler

The ClusterProfiler (v4.10.0) [51] (https://github.com/YuLab-SMU/clusterProfiler) R package was utilized to study enriched pathways (GO and KEGG). A list of differentially expressed genes was used with log2FC > 0.25 and adjusted p value < 0.05. Genes with positive log2FC values were used to identify pathways enriched in different cell types and FB phenotypes using compareCluster() function. For pathways enriched in different groups, or genes obtained from correlation analysis using enrichGO() and enrichKEGG() functions as specified in the figures. Biological pathways "BP" subontology and qvalueCutoff = 0.05 was used in the analysis. The Simplify() function on the enrichResult was used to merge redundant pathways with the following parameters (cutoff = 0.7, by = "*p* value", select_fun = min). In addition, to specifically confirm the enrichment of circadian genes in the comparison of DCM versus ICM after adjusting for fibrosis burden, we tested the GO terms GO:0048511 ("rhythmic process") and GO:0032922 ("circadian regulation of gene expression"). Genes with log2FC > 0.25 and adjusted *p* value < 0.2 were used as the input gene list, while all genes tested in the DESeq2 model were used as the background set. Fisher's exact test (equivalent to a hypergeometric test) was applied to quantify enrichment by constructing a 2×2 contingency table of overlapping and non-overlapping genes between the DEG list and the circadian gene set. Enrichment was considered significant at *p* value < 0.05.

Trajectory analysis and gene modules by monocle3 and Slingshot

Trajectory analysis of FB phenotypes were performed using monocle3 (v1.0.0) R package [52]. A Seurat object of clustered FB was converted to a monocle3 object and Seurat clusters and UMAP was used to build the trajectory. A principal graph was fitted using the learn_graph() function, and FB nuclei were assigned a pseudotime value using order_cells() function based on their projection on the principal graph learned after choosing FB0 as the root state.

The graph_test() function was utilized to find genes that vary between groups of FB nuclei in the UMAP plot. This function is based on Moran's I spatial autocorrelation analysis and was performed with "principal_graph" neighbor graph and q-value threshold of 0.05. Then, the varying genes detected in the previous step were grouped into modules through Louvain community analysis with find_gene_modules() function, which principally runs UMAP on the genes instead of cells. Parameters were set to default. The modules were clustered either based on 1) condition or 2) phenotype. Results were visualized using pheatmap() (v 1.0.12) and clustered with the Ward D2 method. GeneNMF (v0.9.2) [53], a non-negative matrix factorization approach to extract consensus gene programs, confirmed Module 7 by running multiNMF on ICM samples (k = 4:9, min.exp = 0.05) and deriving metaprograms with getMetaPrograms (metric = "cosine", weight.explained = 0.8, nMP = 13, min.confidence = 0.7), wherein 7/10 Module-7 genes mapped to one metagene with significant resemblance (Fisher test, FDR = 0.038).

To further analyse the trajectories separately during FB0-FB1, FB2-FB5, and FB3-FB4 differentiation, we utilized the Slingshot [54] package (v2.10.0). We subset the corresponding states pairs from the Seurat object and recomputed UMAP embeddings. Lineages were initialized with the resting state as the starting cluster (start.clus = FB0/FB2/FB3), learned via getLineages, and smoothed with getCurves. Before fitting pseudotime models, we applied a stringent per-trajectory gene filter to save computational time: genes were retained if they had > 10 counts in > 1% of cells in the trajectory subset. Dynamic gene expression along pseudotime was modeled with tradeSeq (v1.16.0) [55] using NB-GAMs (fitGAM()), and association with pseudotime was tested by associationTest. Genes were ranked by Wald statistic; smoothed expression was obtained with predictSmooth at 100 pseudotime points and visualized as row-scaled heatmaps (no column clustering). It is important to note that because these datasets comprise chronic, end-stage samples collected across individuals, we interpret the trajectory analysis as a descriptive ordering of continuous gene-expression states rather than evidence of causal cell-state transitions, and any inferred dynamics should be considered hypothesis-generating or supporting evidence for findings reached via other means.

For transcription factor (TF) identification, genes significantly associated with pseudotime were intersected with the curated TF catalog from Lambert et al., 2018 ("The Human Transcription Factors") [56]. For each trajectory, TFs changing along pseudotime were collected; common and unique TFs across the three FB trajectories were then derived by set intersections and visualized by plotting pseudotime vs. smoothed expression.

Correlation analysis

Pearson correlation between the gene of interest and all other genes was calculated using cor.test() function after removing lowly expressed genes using aggregated data per sample. A *p* value estimate was also reported with the same function. The same approach was followed in calculating correlation of gene expression with fibrosis. Genes were considered correlated when pearson > 0.5, and *p* value < 0.05 unless otherwise specified elsewhere.

Cellular communication by NicheNet and CellChat

Analysis was performed using the 'nichenetr' R package (v2.0.0) as described recently [57]. NicheNet uses a prior model based on integrating previous knowledge on ligand-to-target signalling pathways. Gene expression was filtered for min.pct = 0.1 and log2 fold ratio > 0. 5 in both analyses. To predict ligands responsible for activating the resting FB states (FB0, FB2, and FB3), genes positively correlated with fibrosis within each of these resting FB states were used as geneset of interest (the genes that are hypothesized to be expressed as a result of ligand activity), and genes positively correlated with fibrosis from all cardiac cells in HF were considered as sender (ligands that would cause such change in gene expression). FB0, FB2, and FB3 were considered as the target. Genes were considered correlated when pearson > 0.5, and p value < 0.05. The 'predict_ligand_activities' function was used, and the top upstream ranked ligands were chosen based on the corrected AUPR (Area Under the Precision-Recall Curve) values. A heatmap representing a ligand-target network was created using data of best ranked ligands and their corresponding target genes found within differentially expressed genes between the condition of interest and the reference condition.

CellChat (v1.1.3) was employed to confirm our previous results by checking communication probabilities from the main cell types and FB states on FB0, FB2, and FB3 that were upregulated in HF. A CellChat object list was made by running the default parameters on HF and NF datasets separately. Then, a merged cellchat object was made from the list after lifting the objects to ensure comparison between the datasets (due to differences in cell composition). netVisual_bubble() was utilized to compare the communication probabilities of ligand-receptor pairs from a group of cells to another group of cells. Default parameters were used.

Spatial transcriptomic data analysis

Raw histology images and processed Seurat objects of each slide were downloaded from [31]. For the 1st approach, FB states markers and major cell type markers from our snRNAseq dataset was obtained (avg_log2FC > 0.5 for FB and avg_$\log_2$FC > 2 for major cell types) and genes module scores of each cell state/type were calculated for each spot using AddModuleScore() function in Seurat. A module score is a measure used to quantify the activity or expression of a predefined set of genes. A high module score of a specific geneset (FB states/cell types) within each spatial spot thus suggests the presence of that cell state/type within that spot. For the 2nd approach, we employed the DOTr package (v0.9) [58], which facilitates flexible feature transfer to spatial omics data, to integrate our snRNA-seq data with processed spatial transcriptomics datasets from [31] using default parameters unless specified. We used our NF snRNAseq dataset with cardiac cell type and main resting FB states to deconvolute the spots in each of the NF slides ($N = 4$). Similarly, we used our HF snRNAseq dataset with cardiac celltypes and FB states to deconvolute each of the visium fibrotic tissue slides ($N = 6$). The reference dataset was created using setup.ref function, and the respective target spatial data was processed by setup.srt function. Dot object was created with create.DOT function, and deconvolution for each spatial slide was performed by run.DOT.lowresolution function (ratios_weight = 1, max_spot_size = 20). we evaluated the deconvolution results using three complementary approaches. First, we compared group-level means, confirming that the deconvoluted proportions were consistent with expected biology (e.g., decreased cardiomyocytes in fibrotic regions; see Additional file 2: Table S10). Second, we assessed spatial correspondence with histology, where cell-type enrichments aligned with known anatomical structures, such as cardiomyocyte-rich regions and vascular niches. Third, we evaluated the method using the published human heart snRNA-seq atlas from Kuppe et al. as a reference, applying the same DOT parameters. We then calculated Spearman correlations between the cellular compositions of the atlas and the deconvoluted spatial data. These showed high concordance, comparable to that reported in the original study (see Additional file 1, Fig. S8a). The cell-state and cell-type abundance estimates generated by DOT for all slides were used as input for mistyR (v1.10.0) [14] to assess the influence of the abundance of each primary cell type on the abundance of FB states and other major cell types. The data were modelled using a multiview framework that considered two distinct spatial contexts: (1) an intra-view, which examines relationships within the same spot using create_initial_view() function, and (2) a juxta-view, which accounts for relationships between immediate neighbouring spots using add_juxtaview(neighbor.thr = 155) function. The model output includes importance scores, where higher values indicate that the abundance of a specific cell type (target) can be spatially predicted by another cell type (predictor). The median standardized importance scores from each view, aggregated across all slides, were interpreted as indicators of spatial dependencies between cell types-such as colocalization or mutual exclusion. An importance score threshold of 0.5 was used to identify meaningful interactions. It is important to note that these interactions are correlative in nature and do not imply causal relationships. The resulting spatially resolved cell type maps were validated against known anatomical structures and histological data.

Histology for fibrosis and collagen quantification

OCT-embedded tissue block samples from the same biopsy tube as used for sequencing were utilized to maintain a strong correlation between transcriptomic data and fibrosis quantification. Tissue slices, 5 µm in thickness, were stained using PicroSirius red dye (PolySciences) for collagen assessment. These sections were then mounted and visualized under a Zeiss Axioplan microscope using a 20 × magnification objective. Images were managed and analysed using Zeiss ZEN 3.7 software. The extent of fibrosis was quantified through ImageJ (FIJI) software, and results were presented as the percentage of the area covered by the dark staining of fibrotic regions.

Histology for top FB states markers from Human Protein Atlas

Proteins encoded by top markers for each state were checked in Human Protein Atlas (https://www.proteinatlas.org/) [59]. Antibodies are labelled with DAB (3,3'-diaminobenzidine) and the resulting brown staining indicates where an antibody has bound to its corresponding antigen.

Data visualization

All visualizations were performed in R. Most plots were prepared using the same packages utilized to perform the analysis. Some plots were visualized using ggplot2 (v3.5.1) or scCustomize (v 2.0.1).

Statistics and reproducibility

No formal sample size calculations were conducted as this is an exploratory study. Sample size was based on heart and tissue availability across the different groups and was chosen with a design for deep sequencing to recover high cell numbers. Each sample in each condition represents a unique biological replicate. No samples were excluded from the analysis. All analyses were performed using R Software, 4.3.2. Statistical tests used and number of biological replicates per condition are indicated in the legends. Data were considered significantly different when the p value or adjusted p value padj (or Q) were < 0.05. Where relevant, individual sample data are shown in the supplemental figures. For image analysis, the investigator was blinded.

Results

Global cellular landscape and changes with heart failure

We performed snRNA-seq (10x Genomics) on nuclei isolated from cardiac tissue (mid-myocardium) snap-frozen at the time of transplantation, representing these HF aetiologies (ICM; $N = 5$; DCM; $N = 6$). Data was compared with closely aged-matched non-failing donor hearts (NF; $N = 4$) (Fig. 1a). Five samples taken from a visibly scarred region of ICM hearts were also analysed (ICM-scar; $N = 5$, 3 of which were matched with ICM samples) (Fig. 1a). Samples were distributed between male and female (Additional file 2: Table S1). NF samples were demultiplexed based on sex genes. As indicated by Sirius Red staining, fibrosis was more prevalent in HF samples, particularly scar, although substantial variability was detected (Fig. 1b-c). To optimize capture of lowly expressed genes, cell types and cell-type heterogeneity within each sample, we targeted 8,000 nuclei per sample at a read depth of 80,000 reads per nucleus. After quality control, 142,024 qualified nuclear transcriptomes remained that had a median of 2,288 genes and 5,672 counts detected (Additional file 1: Fig. S1a and b for per sample data).

Louvain clustering of the snRNA-seq dataset yielded 18 clusters (Fig. 1d), representing 13 different cell types, which were annotated according to their expression of cell specific markers (Additional file 1: Fig. S1e), top expressed genes (Additional file 2: Table S2), and conventional biological functions using Gene Ontology pathways (Additional file 1: Fig. S1f). Amongst these clusters, FB were most abundant, accounting for ~ 35% of all cells (Additional file 2: Table S3), followed by CM and endothelial cells (EC), which were also highly prevalent. The remaining nuclei included myeloid cells (MC), pericytes, smooth muscle cells (SMC), lymphoid cells, endocardial, lymphatic EC, mast, neuronal, and adipocytes (Fig. 1d). While MC mainly comprised macrophages, B and T cells were identified in distinct clusters. Confirming successful nuclear isolation and data processing, all cell types contributed to all conditions, sex, and sequencing batches (Additional file 1: Fig. S2a-c).

Next, we investigated how cell type composition changed in HF (Fig. 1e, Additional file 1: Fig. S2d, and Additional file 2: Table S4). While the presence of fibrosis suggested increased FB abundance in HF, this was not observed in the compositional analysis (see Additional file 1: Fig. S2d for per heart data). Differential gene expression (DEG) analysis of pseudo bulk snRNA-Seq data identified FB as the cell type showing the greatest transcriptional alterations in all HF groups compared to NF (Fig. 1f). This substantial alteration in FB gene expression was also apparent in correlation analysis, where expression of fibrosis-related genes (*TGFB1*, *COL1A1*) and enrichment of cell pathways (RNA machinery) correlated positively with fibrosis determined histologically (Additional file 1: Fig. S3a-c and Additional file 2: Table S5). The greater number of DEG in FB was retained after downsampling of data to achieve equivalent numbers of all cell types, indicating that this higher number of DEG was not related to the greater proportion of FB in the myocardium (Additional file 1: Fig. S3d-e). CM exhibited the next greatest number of DEG in all HF regionsCM-related gene pathways, including muscle development,

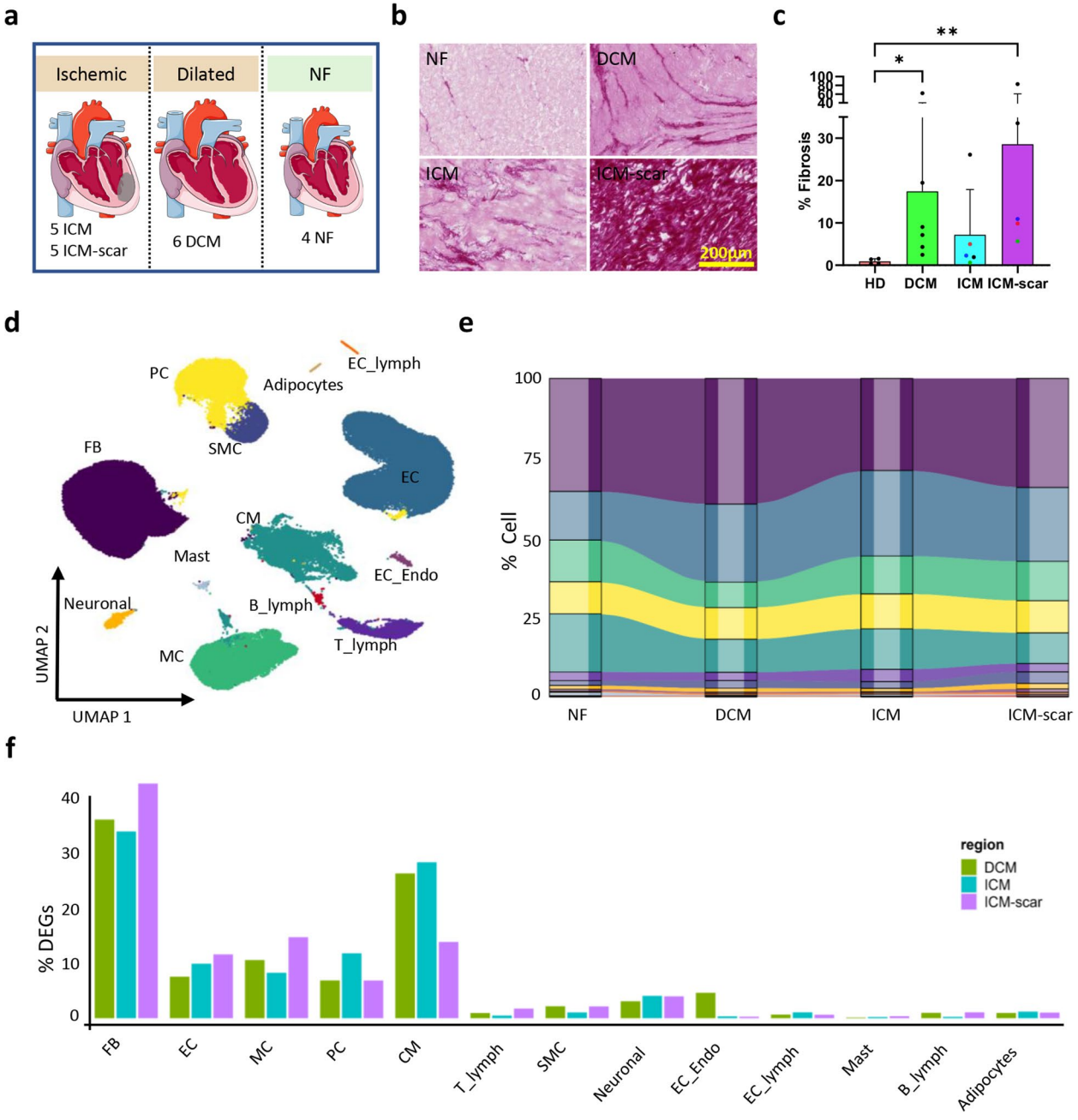

Fig. 1 Cellular distribution and contribution to the failing human heart. **a** Overview of human hearts and aetiologies for cardiac tissue samples, taken from the mid myocardium of the LV free wall. NF, non-failing unused donor heart, DCM dilated cardiomyopathy, ICM ischemic cardiomyopathy. In ICM hearts, samples were taken from non-scar and scar tissue. Adapted from smart.servier.com. **b** Images of fibrosis near the regions sampled for RNA sequencing. Sirius red staining. **c** Fibrosis quantification as percentage of Sirius Red staining of the total area. Data represents mean ± SD. Kruskal–Wallis test used. Dunns multiple comparison test was used. *, p value < 0.05; **, p value < 0.01. **d**. 2D visualisation (UMAP dimensionality reduction) of pooled data from all samples (142,024 nuclei), highlighting different cell types. **e** Relative abundance of each FB cluster across disease groups (NF: $n = 4$; DCM: $n = 6$; ICM: $n = 5$; ICM-scar: $n = 5$), measured in the integrated snRNA-seq dataset (same colour code as in panel **d**). Cluster proportions were analyzed using the speckle R package. Benjamini–Hochberg FDR correction was used. No statistical significance was observed after correction. **f** Percentages of differentially expressed genes (DEGs) in each cell type comparing every HF condition vs non-HF determined in pseudo-bulk analysis. CM; Cardiomyocytes, FB; Fibroblasts, EC; Endothelial cells, SMC; Smooth muscle cells, MC; Myeloid cells

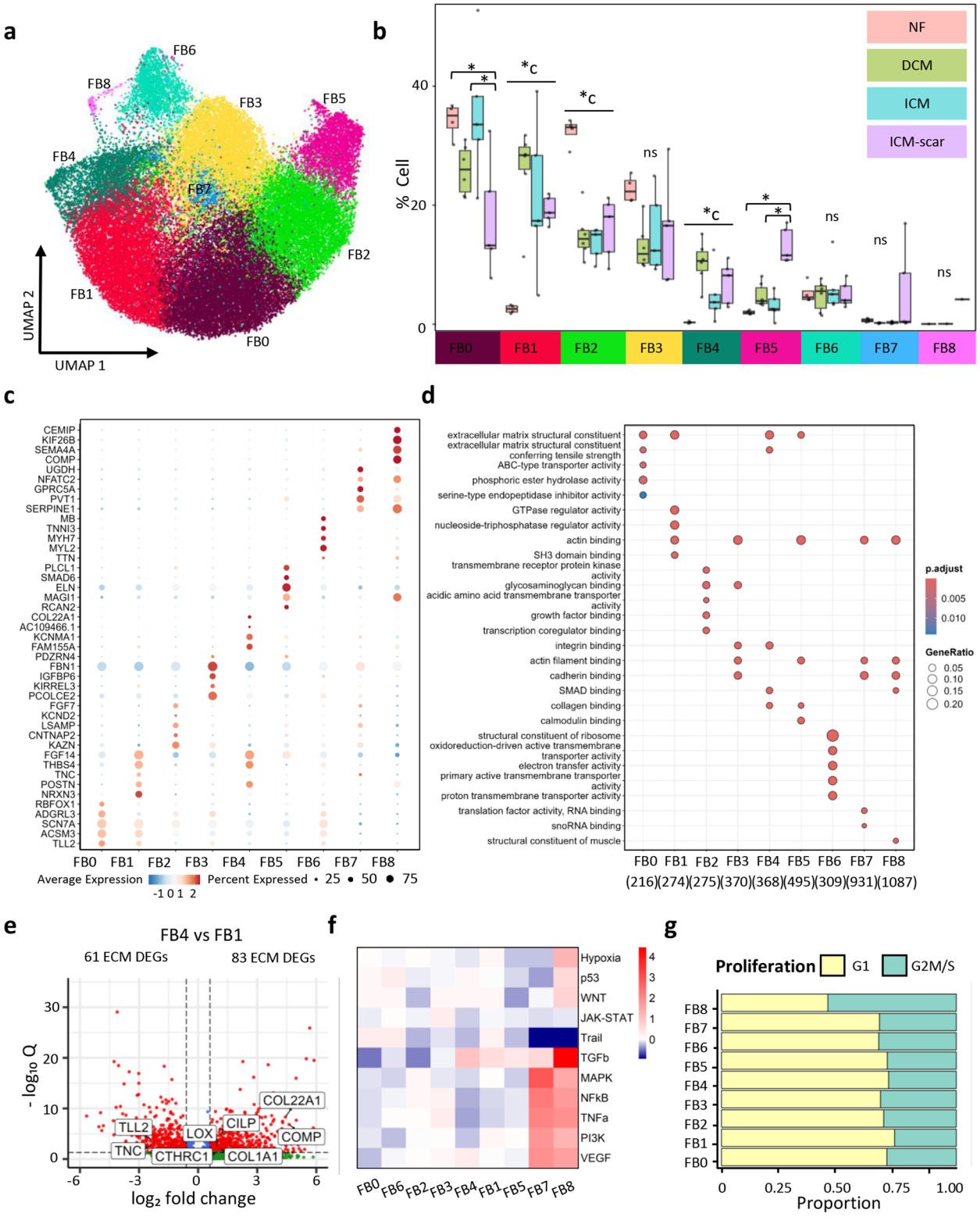

Fig. 2 (See legend on next page.)

(See figure on previous page.)

Fig. 2 Fibroblast heterogeneity within non-failing and failing human hearts. **a** 2D visualisation (UMAP) of FB subclustering (49,308 nuclei), highlighting identified FB states. **b** Relative abundance of each FB cluster across different conditions, as measured in the integrated snRNA-seq dataset. Cluster proportions were analysed with the speckle R package. Benjamini–Hochberg FDR correction was used (NF: $n=4$; DCM: $n=6$; ICM: $n=5$; ICM-scar: $n=5$). *c indicates all HF groups are significant compared to NF with FDR < 0.05. * indicates significance for the selected comparisons with FDR < 0.05. **c** Dot plot showing the top five marker genes of each subcluster. Dot colour and size correspond to the expression of each gene and the proportion of cells expressing each gene, respectively. **d** The top five enriched Gene Ontology pathways of each FB cluster. The number in parenthesis indicates the number of DEGs. **e** Volcano plot showing FB1 (left side) and FB4 (right side) differentially expressed genes. Some matrix genes are labelled. Q; adjusted *p* value. **f** Heatmap showing enrichment of PROGENy pathways in different FB clusters. **g**. Bar plot showing FB proliferation proportion in different regions based on cell cycle scoring

contraction, and fatty acid oxidation, showed negative correlations with histological fibrosis (Additional file 1: Fig. S3a-c and Additional file 2: Table S5). Together, these data highlight FB as a highly plastic cell type, which undergoes substantial remodelling during HF.

Clustering of fibroblasts into subpopulations

Based on their transcriptomes, cardiac FB have been subdivided into multiple substates, which correlate with different functional properties and activation state [26–31, 60]. We therefore investigated whether the transcriptomic changes in FB could be explained by alterations in FB substate identity and proportions. Unsupervised sample-level analysis of FB showed that aetiology and location, i.e. DCM, ICM non-scar and ICM-scar, are the main determinants of sample separation (Additional file 1: Fig. S4a). Sub-clustering of FB from NF, ICM, DCM and ICM-scar ($n=49{,}308$ nuclei) identified 9 FB substates that varied in their presence and relative proportions according to the biological condition (Fig. 2a-b; Additional file 1: Fig. S4b presents data for each heart). FB0, FB2, and FB3 dominated in NF tissue.

In HF, while FB0, FB2, and FB3 remained major contributors, emergence of FB1 and FB4 across all HF groups, resulted in an increase in the overall heterogeneity of HF FB. FB5 also increased significantly in ICM-scar. FB7 and FB8 were uniquely expressed in ICM-scar, albeit at a very low abundance. FB6, was equally abundant across all conditions.

Resident FB populations of the NF heart

To investigate the relevance of each FB state to aetiology, their functional phenotype was first investigated by analysis for enrichment of marker genes (Fig. 2c and Additional file 2: Table S6) and pathways in the Gene Ontology (GO) and Kyoto Encyclopedia of Genes and Genomes (KEGG) relative to all other clusters in the dataset (Fig. 2d, Additional file 1: Fig. S4c, and Additional file 2: Table S7 and 8).

The dominance of FB0, FB2 and FB3 states in NF and their reduction in pathology categorized these FB states as contributors to the normal functioning of the NF heart. Moreover, these proposed resting FB populations expressed genes involved in the housekeeping function of FB to deposit and remodel the ECM. Specifically, FB0 is characterized by expression of genes and pathways associated with extracellular matrix (ECM) structure, and of its remodelling i.e. the metalloendopeptidases, and hydrolase activities. With 216 enriched genes, this FB state showed the least specialization in its transcriptional remodelling in HF, including between NF and Scar (compared to other clusters. Figure 2d x-axis in parentheses), suggesting it represents a more resting FB state. FB2 was enriched for genes encoding the growth factors FGF7 and FGF10, complement, FOS-related genes, and BMPER, while matrix-related genes were less expressed. These genes contributed to upregulated pathways related to growth factors, glycosaminoglycans, glucocorticoid receptor binding, tyrosine kinase activity, and MAPK, FoxO, and JAK-STAT signalling. Together, the patterns of expressed genes and enriched pathways suggest a more signalling/regulatory function for this state than in ECM secretion. FB3 is distinguished by a signature of gene expression and pathways involved in ECM-modulation, including the procollagen C-endopeptidase enhancer (*PCOLCE2*) involved in collagen maturation, and fibrillin 1 (*FBN1*), and pathways involved in ECM and ECM components, actin, cadherin, and integrin binding. Together, these findings underline the important role of this cluster in matrix modulation and mechanosensing.

Activated FB states in HF

While the abundance of both FB1 and FB4 was low to negligible in NF, these states were significantly more abundant in HF across all groups. Indeed, FB1 emerged as one of the dominant FB states in HF. Enrichment of FB1 and FB4 for expression of genes associated with FB activation including *POSTN*, *FAP*, *TNC*, and *THBS4* and in pathways related to ECM tensile strength is supportive of these FB states being of an activated phenotype. To probe the specific contributions of these 2 states to HF-associated fibrosis, we analysed differential expression of genes (pseudobulk data) between them focusing on a curated set of ECM-related genes (termed the matrisome) [49]. A significant number of these genes was differentially expressed (0.5 $\log_2$ fold change cutoff, total 144 ECM-related DEGs, 61 in FB1 and 83 in FB4) (Fig. 2e). FB1 enriched genes included tenascin C (*TNC*), encoding a matricellular protein with functions including adhesion of CM to ECM in the BZ after MI [61, 62] and tolloid like

2 (*TLL2*), encoding a procollagen C-proteinase member that facilitates the proteolytic processing of pro-LOX to LOX [63]. Genes upregulated in FB4 vs FB1 including *COL22A1*, *CTHRC1*, *COL1A1*, *CILP*, and *COMP* that contribute to TGF-β signalling, ECM deposition and MyoFB activation are consistent with FB4 being of a more activated state than FB1 [9, 24, 32, 64–67].

FB1 and 4 also express unique patterns of genes unrelated to fibrosis. FB1 expresses *NRXN3*, a gene encoding a synaptic cell adhesion molecule critical for maintaining neural connections and aiding cell migration. FB4 shows increased expression of genes encoding proteins involved in membrane excitability and calcium handling, including *FAM155A*, which is found in a complex with the non-selective cation channel *NALCN*, and of *KCNMA1*, a calcium-regulated potassium channel.

Taken together, the analysis identified two activated FB states in HF. Differences in the degree of activation of fibrosis-related genes and the presence of uniquely expressed genes suggest however functional specialization or differences in origin and/or tissue location of these two FB states.

Unique FB states characterize the ischemic scar region

Given the central role of FB in sustaining cardiac integrity after MI, we also analysed FB remodelling in the ICM-scar. This region exhibited the greatest diversity of FB where, compared to HF, 2 additional substates, FB7 and FB8 emerged, and the abundance of FB5 significantly increased. FB7 was however only increased in abundance in 2 out of 5 samples and FB8 in 1 of the 5 scar samples (Additional file 1: Fig. S4b). Despite their decreased abundance relative to NF, FB0 and FB2 remained significant contributors to FB in ICM-scar.

Properties of ICM-scar-enriched FB states were next investigated. FB5 was enriched for genes associated with interactions with the ECM and the cytoskeleton (e.g., *MAGI1, MYH10, ACTA2*), and ECM modulation (e.g., *ELN, COL21A1*), which contributed to the pathways 'actin filament' and 'collagen'. Genes with a more signalling function were also enriched in FB5, including those that inhibit the calcineurin and TGF-β pathways. Consistently, calmodulin binding was enriched in this pathway analysis. FB7 and FB8 exhibited the greatest number of enriched genes (931 and 1,087 respectively, compared to 216–495 in other cell states; Fig. 2d), indicating their transcriptional diversity and substantial remodelling during scar formation, and suggestive of greater specialization. These FB states show some similarity with each other in gene enrichment, including *SERPINE1* and *NFATC1* and *2,* and in pathways involved in inflammation and hypoxia, including those involving HIF-1 and TNFα signalling.

The significant transcriptional changes and low apoptosis gene signature (least enrichment of Trail pathway from PROGENy; Fig. 2f) in FB7 and FB8 also suggested a link between these states and cellular senescence. Consistently, cell cycle gene-scoring detected a general increased proliferation in HF across all groups, including scar (increased G2M/S vs G1) (Additional file 1: Fig. S4d), whereas FB8 and to a lesser extent FB7, exhibited a decrease in G2M/S phase genes, suggesting lower cell proliferation (Fig. 2g). Further supporting the senescent phenotype of FB7 and 8, they showed enrichment for genes associated with the senescence-associated secretory phenotype (SASP; for example IL-6, IL-8, and MMPs) [47] (Additional file 1: Fig. S4e).

FB6 was present in all groups with no alteration in proportion between conditions. This FB state was enriched in gene sets related to antigen presentation roles, including those associated with major histocompatibility complex, class I and stress induction, such as Human Leucocyte Antigen (HLA), Heat Shock Proteins (HSP), in addition to some genes associated with CM (Additional file 1: Fig. S4f). As this FB state was not influenced by disease state, we did not examine it further.

Together, these data further demonstrate the unique nature of scar tissue containing FB in advanced stages of maturation and senescence, as well as containing resident and activated FB.

Comparison of identified FB states to published cohorts

Previous single-cell/nucleus RNA-seq studies of human cardiac cells have also assigned FB to multiple substates. Given that our aim was to identify FB phenotypes specific to different aetiologies, including scar, rather than project our FB onto established states that may not span the diversity of our sample groups, we assigned FB in an unbiased manner. To contextualize our findings, we compared marker genes from published cohorts [16, 26, 29, 31, 44, 60, 68, 69] to our states using the Tversky index (for detailed one-to-one comparisons, see Additional file 1: Fig. S5; extensive figure legend). FB0 was predominantly described as a basal/lipogenic state and aligned with a universal COL15A1$^+$ FB state; FB2 was more consistent with immune/chemokine-responsive state; FB3 reflected a matrix-modulatory state and overlapped with PI16$^+$ universal FB; FB1 and FB4 were mostly captured as a single activated/myoFB state; FB5 also mapped to myoFB state; FB6 showed similarities spread across multiple, variably defined clusters; and FB7 and FB8 were closest to a SERPINE1$^+$ FB population. Supporting the classification of FB in our dataset, our main FB states (FB0–FB5) mapped closely to the consensus FB clusters defined in the cross-study transcriptional patient map of heart failure [69], with one exception: we resolve two

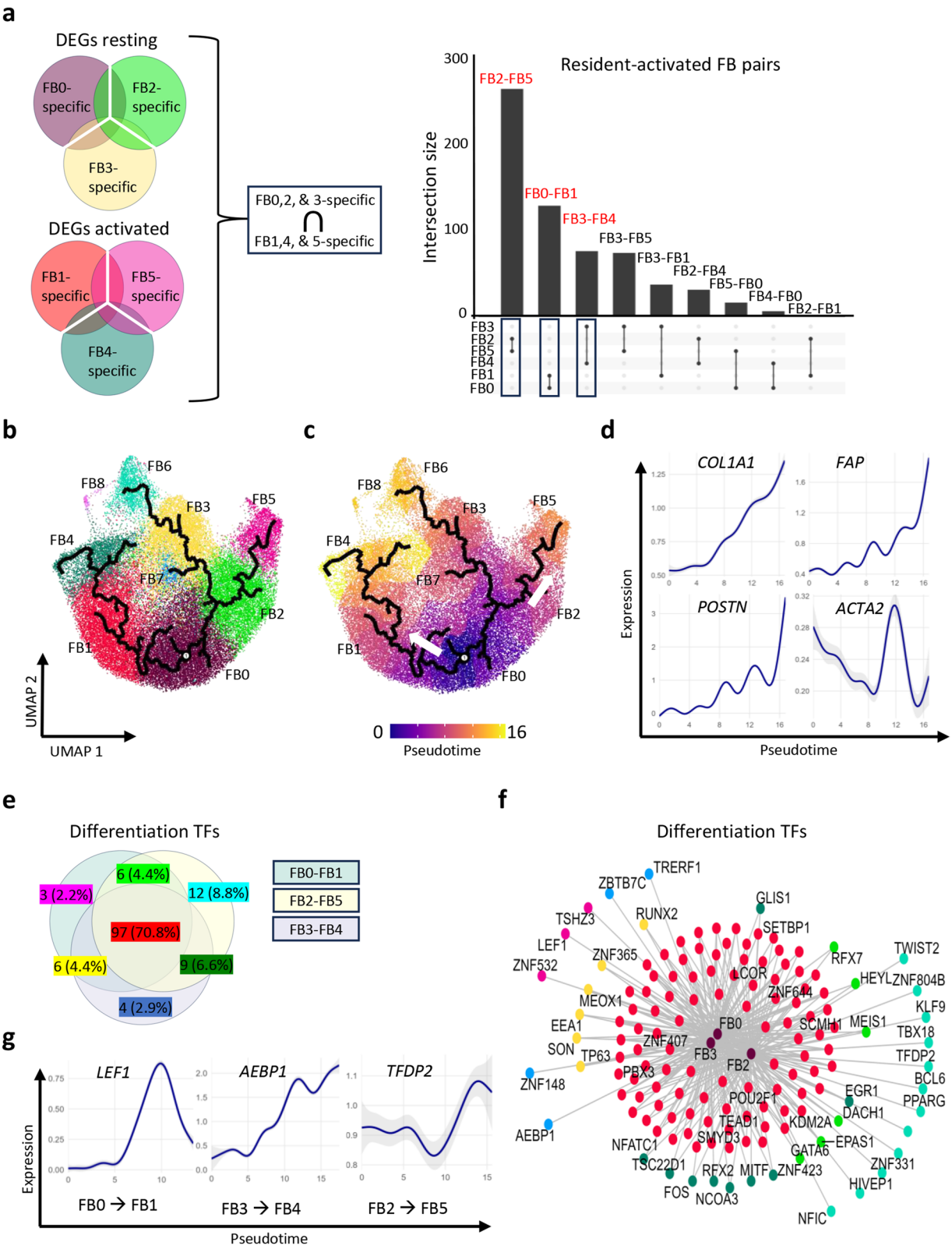

Fig. 3 (See legend on next page.)

(See figure on previous page.)

Fig. 3 Activation of FB is state and context dependent. **a** Left, Schematic of the workflow used in the analysis. Right, UpSet plot visualizing the overlap of differentially expressed genes (DEGs) between activated and native fibroblast states. Each set represents a fibroblast state with the number of DEGs identified. Native FB states (FB0, FB2, FB3) and activated FB (FB1, FB4, FB5) were compared separately. Intersections indicate genes shared between clusters compared to the other clusters (log_2 fold change threshold = 0.25). **b** and **c** UMAP visualization of trajectory inferred by monocle3. Cells are coloured by cluster (**b**) or pseudotime (**c**). The centre of FB0 was used as a reference to order cells and assign Pseudotime values for each cell. **d** Expression levels of selected genes along pseudotime (*COL1A1*, *FAP*, *POSTN*, and *ACTA2*). **e** Venn diagram grouping of the associated transcription factors with pseudotime along each trajectory. **f** Individual transcription factors that are shared and specific between trajectories. The colour code relates to the groupings shown in (**f**, **g**). Transcription factor expression over pseudotime

distinct activated FB states (FB1 and FB4), whereas these two states fall within a single activated state in that study.

Different activated FB states arise via distinct trajectories from different resting states

The dominance of FB0, FB2, and FB3 in NF, and the increases in FB1, FB4, and FB5 in HF suggested that states present in HF derive from those in NF. To test this, we investigated shared patterns of gene expression between resting and activated FB states. To these ends, we first separately identified the genes specifically enriched amongst each of the resting and activated FB states and then intersected these to identify the associated resting-activated FB state pairs (Fig. 3a). The FB0-FB1 and FB2-FB5 pairs shared the greatest number of enriched genes, consistent with trajectories from FB0 to FB1 and FB2 to FB5. FB3 showed the most overlap with FB4, but with close numbers to other activated states. Similar trajectories were detected in by constructing a matrix of DEGs of each FB state vs all (Additional file 1: Fig. S6a).

To further explore these potential pathways of differentiation, avoiding introducing bias through exclusion of any FB states, we performed a trajectory analysis (Fig. 3b). This analysis revealed a trajectory initiating at FB0 that passed through FB1 and ending in FB4 and another progressing from FB2 towards FB5. FB3 did not directly progress towards FB4 but was linked to a branch point with FB0 and FB2, in addition to FB6 and FB7. Pseudotime of differentiation was higher when passing through FB1 and FB4, consistent with the notion that FB1 arises from FB0 and that FB4 is a more differentiated phenotype than FB1 (Fig. 3c). Of note, FB5 showed a relatively lower pseudotime compared to other activated FB, suggesting its greater similarity to resident FB. Furthermore, supporting a relationship between FB differentiation trajectory and fibrosis, FB activation and fibrotic genes (*COL1A1*, *FAP*, *POSTN*) showed increasing expression along the trajectories of differentiation (Fig. 3d). Of interest, *ACTA2* (encoding alpha smooth muscle actin, α-SMA) showed increased expression in the middle of the trajectory followed by a rapid decline, in line with previous data that α-SMA is lost in advanced disease [9].

Although a direct link between FB3 and FB4 or FB1 was not detected in our analysis, a transition from a resting state similar to FB3 to more activated states has been described previously [31], and similarities in gene expression in atherosclerosis studies support such a link (Additional file 1: Fig. S6b).

To investigate mechanisms underlying the different differentiation paths of each resting state, we analysed gene expression along differentiation trajectories (pseudotime) identified by Slingshot for FB0 to FB1, FB2 to FB5, and FB3 to FB4. This analysis identified many DEG that were common to all trajectories (66.8%), as well as unique genes and pathways (Supplemental data, Fig. 6c-e). Next, we identified transcription factors that were differentially expressed along the studied trajectories (Fig. 3e). Again, many were common to all trajectories (70.8%), while others were unique. While some of the identified transcription factors have been previously implicated in FB differentiation and cardiac fibrosis (*AEBP1*, *MEOX1*, *RUNX2*, *TEAD1*), others have not (eg. *LEF1*, *TFDP2*, *GLI2*) (Fig. 3f). Specifically, *LEF1* was specific to FB0-FB1 differentiation, *AEBP1* to FB3-FB4, *TFDP2* to FB2-FB5, and *GLI2* was common to all (Fig. 3g and Additional file 1: Fig. S6f). Additionally, *RUNX2* was among the transcription factors specific to FB0-FB1 and FB3-FB4 only, *TSC22D1* for FB2-FB5 and FB3-FB4, and *GATA6* for FB0-FB1 and FB2-FB5 (Additional file 1: Fig. S6g i-iii).

Together, these findings demonstrate that FB differentiation follows a path specific to the resting state.

Conserved and distinct ligands govern resident fibroblast activation

Beyond their transition to activated states, resting FBs exhibit differences in their transcriptomes between NF and HF (Additional file 1: Fig. S7a) that represent the initial stages of their activation. We therefore investigated the identities of the paracrine cues that could instigate the activation of these resting (FB0, FB2, and FB3) FB states. To this end, we used NicheNet to identify relevant ligand-receptor interactions. To restrict the analysis to the analysis of fibrosis (treating fibrosis association as a surrogate for FB activation), genes from all cell types that are positively correlated with fibrosis were considered as potential ligands (data from Additional file 1: Fig. S3 and Additional file 2: Table S5), and within each resting FB cluster, genes that were positively correlated with fibrosis were considered as potential targets (Fig. 4a and Additional file 2: Table S9).

Across the three resting FB states, this analysis yielded an expected repertoire of ligands involved in fibrotic remodelling, although not all were found in all states, and in some cases, were unique to one state (Fig. 4b). Notably, TGF-β, exhibited high regulatory potential for multiple targets in FB0 and FB3, including its receptor TGFβR1, collagens and periostin but was not prioritized as a ligand for FB2 activation. *CTGF*, *SERPINE1*, *FN1*, *PROS1*, *FGF1*, and *COL1A1* however were common to all three FB states with high potential for regulating expression of target fibrotic genes. Other activation ligands were specific to individual states. For example, the junction adhesion molecule *JAM2* for FB0, adhesion molecule *ICAM2* for FB2, and the TGF-β superfamily member *INHBA* for FB3. These ligands were enriched in pathways related to chemotaxis, migration, and proliferation (Fig. 4c), corroborating the understanding that fibrosis involves cell recruitment, expansion, and invasion.

Further analysis of ligand-target relationships for each FB state revealed common targets for ligands, suggesting a requirement for this interaction for FB activation irrespective of state (Fig. 4d-f and Additional file 1: Fig. S7b-c). For example, *CTGF*, *SERPINE1*, *TGFB1*, *PROS1*, *FGF1*, and *COL1A1* were identified as key players influencing fibrotic genes (Fig. 4d-f). Many target genes were common between FB0, FB2, and FB3 (27.6%), while others were specific to each state (Additional file 1: Fig. S7b). GO pathway analysis of these genes showed common pathways across all FB states including adherens junctions, SMAD and actin binding (Additional file 1: Fig. S7c). Histone demethylase activity and phosphatidylcholine binding were specific to FB3 targets, while response to peptide hormones and protein dephosphorylation were specific to FB2 targets. FB0 did not have any specific GO pathway.

The cell type origin of key ligands was next identified through analysis of their expression across the cell types of the heart, and whether they were differentially expressed in HF. Although many cardiac cell types contributed, FB and EC were the greatest ligand expressing cell types across all conditions (Additional file 1: Fig. S7d). However, and suggesting a dominant role for autocrine signalling in FB activation, activation ligands were most differentially expressed in FBs during HF (Additional file 1: Fig. S7e). Relatively few activation ligands were differentially expressed during HF in EC on the other hand (Additional file 1: Fig. S7e). Non-FB expressed ligands also exhibited high regulatory potential. For example, *JAM2*, a ligand involved in FB0 activation, was expressed in EC and CM and upregulated during HF. *PDGFB*, involved in FB2 activation, was expressed in myeloid cells and upregulated during HF, while *FGF1*, involved in FB3 activation, was primarily found in pericytes and smooth muscle cells (SMCs) and upregulated during HF. This suggests distinct interactions between FB0 and CM, FB2 and immune cells, and FB3 and the vasculature.

We also examined cell–cell interactions between all cardiac cell types and the ligands involved without a priori prioritization of ligands and targets using CellChat (Fig. 4g-h). The findings were overall consistent with the above analysis in that the FB targeting ligands which increased in number and communication probability in HF vs NF significantly overlapped with those identified through a priori prioritization in the above analysis (Additional file 1: Fig. S7f).

Collectively, these findings demonstrate that the activation of resting FB states within the heart is mediated by pathways that are common between states, as well as by pathways unique to each state—the latter suggesting exposure to unique ligands, potentially within a specific spatial niche.

Spatial organization of resident FB states

The presence of several resting FB states that follow distinct activation trajectories involving different ligands to activated states with potentially specialized functions raised the question whether these new FB states were specific to different myocardial locations. We therefore probed the distributions of these FB states by integrating our data with a publicly available spatial transcriptomics dataset of the NF myocardium (Visium, 10 × Genomics) [31] (Fig. 5a-b). First, based on genetic markers, the enrichment of each FB state and major cell type (module score) within a spot of the Visium array was calculated. We then used our snRNA-seq dataset as a reference to deconvolute the spatial transcriptomics data and assigned weights to each cell type/state abundance within each spot using DOTr. After validation of the deconvolution approach (see methods, and Additional file 1, Fig. S8a), MISTy was applied to evaluate the contribution of each cell type (quantified as and importance score), to predict the spatial localization/exclusion of FB states (target) within each spot (intra-view). Analysis regarding the immediate surrounding spots (juxta-view) can be found in the Additional file 1, Fig. S8b-f.

Illustrating the architecture of the samples analysed, CM and SMC showed high module scores in the regions shown histologically to be rich in CM and vessels, respectively, with MC being found in vascular and CM-rich areas (Fig. 5b-c). While both FB0 markers were dispersed across the myocardium, FB3 was substantially enriched around the vasculature. FB2 showed a distribution intermediate between FB0 and FB3; i.e. interstitial distribution but reduced perivascular distribution compared to FB3. Using an importance cutoff of 0.5 applied to MISTy's aggregated estimated standardized importances (median) to detect the most robust dependencies, we then investigated the spatial dependencies between each

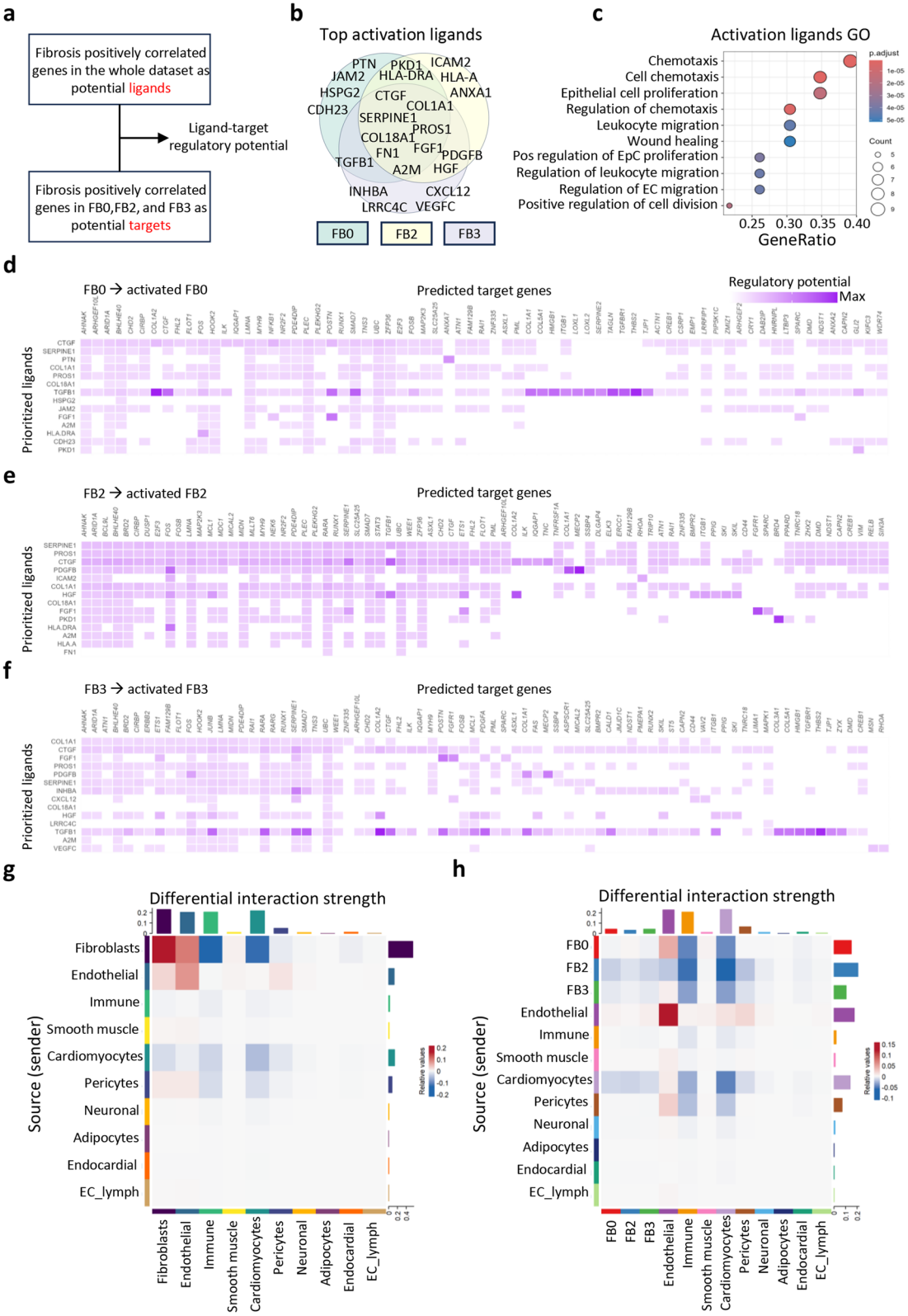

Fig. 4 (See legend on next page.)

(See figure on previous page.)

Fig. 4 Conserved and distinct ligands govern FB activation onset. **a** Schematic of the workflow used in the analysis. **b** Venn diagram grouping the top ligands identified to contribute to FB activation. **c** The top 10 enriched Gene Ontology pathways of activation ligands (shown in b). **d**-**f** NicheNet ligand-target matrix denoting the regulatory potential between predicted ligands and activation target genes (positively correlated to fibrosis) in resident FB0 (**d**), FB2 (**e**), and FB3 (**f**) states. **g** and **h** Heatmap showing differential interaction strength between HF and NF main cell types with FB as one main cluster (**g**) or FB0, FB2, and FB3 states separately (**h**). The blue colour indicates that the displayed communication is decreased in HF, while the red colour indicates that communication is increased in HF compared with NF. The bar plots highlight the sum of absolute interaction strength of each cell type as senders (right) and receivers (top)

resting FB state and between each resting state and other cell types. In line with their distinct histological localizations, SMC location was dependent on the presence of CM and arterial EC (EC_art) within the Visium spots (Fig. 5e), showing colocalization with EC_art and exclusion with CM within the Visium spots (data not shown). Resting FB states showed dependencies with each other, associated with mutually exclusive localization in different spots, particularly when highly expressed (Fig. 5e-f). FB0 and FB2 did not show any dependency with CM, SMC, MC or EC_art, highlighting the absence of direct co-localization within each spot. However, FB3 showed a strong dependency on CM. Analysis of the juxta-view dependency provides information on the co-occurrence or exclusion in the immediate neighbourhood (Additional file 1: Fig. S8b-c). This analysis supported the spatial distribution of FB3, together with SMC in the vasculature but not in CM-rich regions (Additional file 1: Fig. S7e) while the CM-rich distribution of FB0 supports FB0 as being an interstitial FB state (Additional file 1: Fig. S7f).

Confirming localization of FB0 and FB3 to interstitial and vascular regions respectively, protein markers of these states, identified as enriched in the RNA-seq analysis, were localized to these regions in the human protein atlas (HPA). Specifically, as a marker of FB3, we probed the distribution of *VCAN, CD55, FBN1, FBLN2* (encoding proteins Versican, CD55, Fibrillin 1, and Fibulin 2 respectively) and found them to be strongly expressed in the vasculature and not the CM-rich area (Fig. 5g and Additional file 1: Fig. S9a-c). Conversely, the markers of FB0, *LAMB1* and *COL15A1* (encoding Laminin subunit beta 1 and Collagen type XV alpha 1 chain proteins, respectively) were highly expressed in the CM-rich areas and not in the vasculature (Fig. 5h and Additional file 1: Fig. S9d).

Together, this integration of single nucleus and spatial RNA-Seq with histochemical analysis strongly supports the identification of FB0 and FB3 as interstitial and adventitial fibroblasts, respectively.

Spatial organization of FB states after myocardial infarction

We next investigated whether the spatial distribution of the resting FB states was altered in HF and whether the activated states were localized to specific cellular niches, that contributed to their mechanism of activation. Analysis was performed as for NF but using datasets from human cardiac tissue after MI during the late fibrotic phase ($n = 6$) [31]. The tissue remodelling associated with this pathology is illustrated in the histological images (Fig. 6a, left panel) and Visium data used in the analysis where fibrotic areas devoid of CM reflecting the scar are seen (Fig. 6a, right). In the intra-view analysis (Fig. 6b), FB0 and FB1 showed high dependencies on each other. While both FB states were abundant in CM-rich regions, their localizations were mutually exclusive at the level of individual spots (Fig. 6c). Through analysis of cell neighbourhoods (juxta-view), we determined that unlike in NF, FB3 was not dependent on SMC (Fig. 6d-e). Indeed, in contrast to the exclusive peri-vascular distribution seen in NF, FB3 was distributed across the entire fibrotic region of the scar (Fig. 6f). FB1 and FB4 showed dependencies on each other in the juxta-view, which could be seen as a pattern of regional exclusion, where FB1 was more present in CM-rich areas, while FB4 in the scar (Fig. 6g). Moreover, FB2 was dependent on MC showing a pattern of localization with FB3 and MC rich regions (Additional file 1: Fig. S7h). Lastly, FB5 showed localization in fibrotic regions that also contained isolated islands of CM (Additional file 1: Fig. S7i).

Together, these findings strongly point to FB1 arising by transition from the interstitial FB0 state, and FB4 from FB3, which extends its distribution in scar.

FB gene expression signature in scar tissue from ICM

Whether scar FB exhibited features distinct from those in the remote myocardium was next investigated. While our analysis identified altered FB state composition of the ICM-scar, this region remained heavily populated by resting FB states. To avoid these and unique FB7 and 8 states from biasing the identification of transcriptional differences between ICM-scar and remote, we assigned autocorrelated genes (determined using Moran's I statistic as applied in monocle3 [52]) within the UMAP to gene modules and analysed their expression amongst regions, FB states and conditions (Fig. 7a-b, methods, and Additional file 2: Table S11). These modules are segregated between NF, HF and scar. Notably, while ICM-scar showed some overlap with interstitial ICM, it also had a distinct profile, showing strong upregulation of modules 4, 5 and 9, as well as absence of upregulation of module 7, present in HF (Fig. 7b). Supporting the importance of this module 7 to interstitial fibrosis, it was

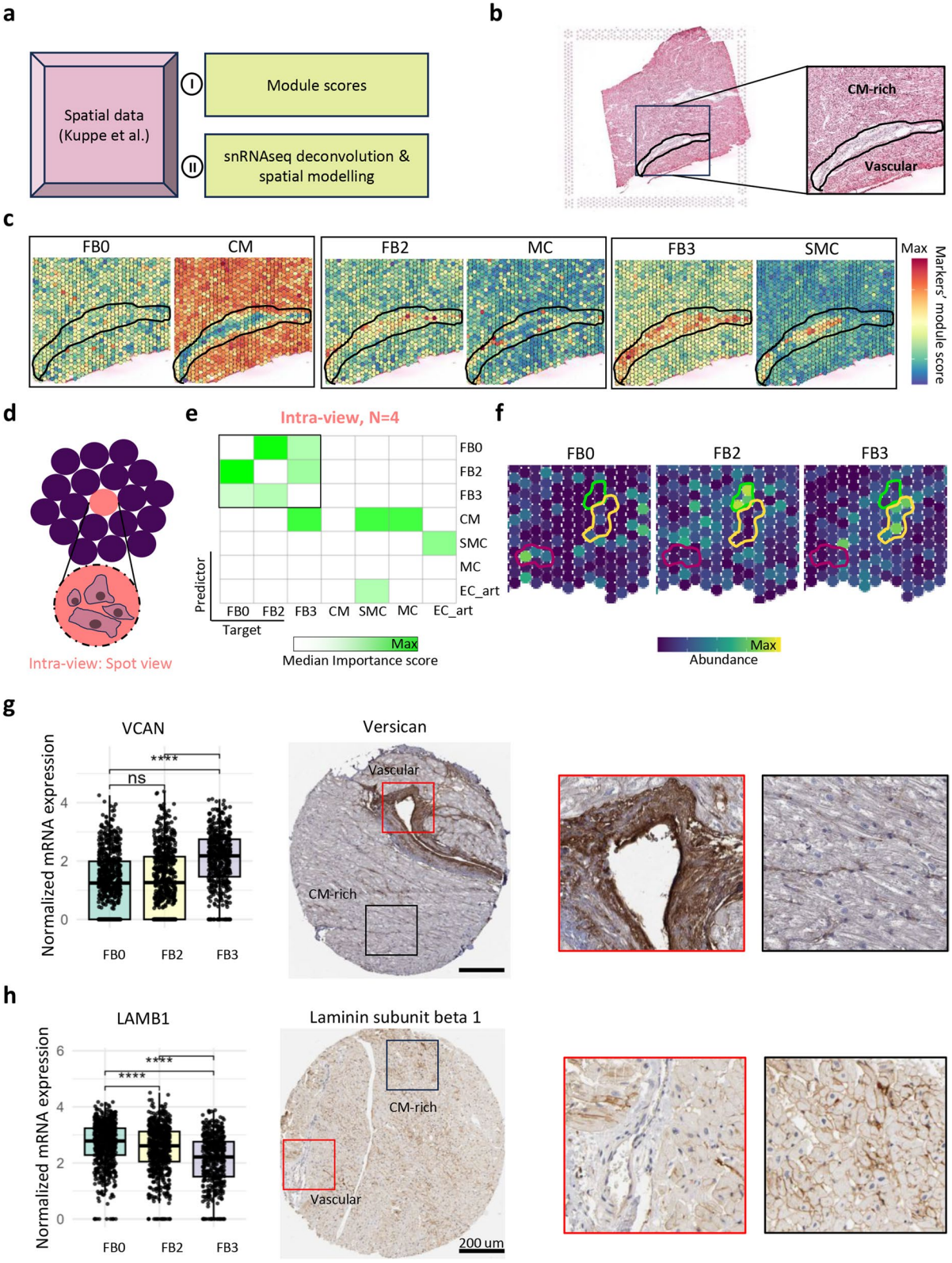

Fig. 5 (See legend on next page.)

(See figure on previous page.)

Fig. 5 Spatial distribution of FB states in healthy myocardium. **a** Schematic of analysis approach using published spatial transcriptomics data from human cardiac tissue to calculate (I) module and (II) prediction scores. **b** H&E staining of healthy myocardial tissue and representative sample (ACH003), highlighting CM-rich and vascular regions. Zoomed area shown in following panels. **c** Spatial visualization of FB0-3, CM, SMC, and MC module scores in ACH003. Black area indicates vasculature, as identified by H&E. **d** Schematic of intra-view modelling used to define within-spot interactions. **e** Median importance of cell-type abundance (predictors) in predicting other cell-type abundances (targets) within a spot (intra-view; $N = 4$ slides). White indicates importance below 0.5 threshold. Green values indicate high importance scores which suggest within spot co-localisation or exclusion. **f** Zoomed region showing deconvoluted FB0, FB2, and FB3 distributions in ACH003, with outlined areas indicating distinct FB states (colours correspond to clusters; Bordeaux is an example of FB0 + spots, green for FB2, and yellow for FB3). **g** Left, Expression of FB3 marker VCAN across FB0, FB2, FB3 (Wilcoxon rank-sum test; ** = significant, ns = not significant). The box shows the interquartile range with the median line. Right, Histological staining of Versican in healthy myocardium (HPA; heart 5145, antibody CAB008979). Red square shows vascular region; black, CM-rich. Brown DAB staining indicates protein expression. Tissue diameter: 1 mm; scale bar: 200 µm. **h** Left, Expression of FB0 marker LAMB1 in FB0, FB2, FB3 (Wilcoxon rank-sum test; ** = significant, ns = not significant). The box shows the interquartile range with the median line. Right, Staining of Laminin subunit beta 1 (HPA; heart 2521, antibody HPA004132). Red square: vascular region; black: CM-rich. DAB staining indicates protein expression. Tissue diameter: 1 mm; scale bar: 200 µm. CM: cardiomyocytes; SMC: smooth muscle cells; MC: myeloid cells; HPA: Human Protein Atlas

enriched in FB0 and activated FB1 (Fig. 7c). These two FB subtype populations were significantly altered in ICM and ICM-scar (Fig. 2b). GO pathway analysis of genes in these modules (Fig. 7d) identified enrichment of metallopeptidase activity and Insulin-like growth factor binding for module 7 genes (Fig. 7e), while scar-enriched modules 3, 4, 5 and 9 showed enrichment in collagen binding, ECM constituents, synapse organization, and leukocyte migration. Most module 7 genes are upregulated in ICM FB compared to both ICM-scar and NF (Fig. 7f), and *ADAMTS19* were transcriptionally specific to FB (Fig. 7g). *TLL2* belongs to the Tolloid family of metalloproteases which processes collagens pro-peptides and through cleaving pro-LOX enhances its activity promoting collagen cross-linking. The presence of this module 7 in non-scar FB was also detected using Non-negative Matrix Factorization (NMF) based method (see methods) [53]. Together, these data suggest that the ICM-scar FB support a more stable ECM, while interstitial ICM FB support matrix turnover and remodelling.

Circadian rhythm disruption in DCM alters FB transcription

Although both DCM and ICM exhibit reactive interstitial and perivascular fibrosis, the patterns and degree of fibrosis between these aetiologies differ ([11]; supplementary data). Leveraging the snRNA-seq analysis of DCM and ICM FB, we probed the phenotype of reactive fibrosis in these aetiologies. This analysis identified a significant number of DEG (300 up and 318 down FDR < 0.05) (Fig. 8a and Additional file 2: Table S12) with ECM organization and response to TGF-β being among the top GO upregulated in DCM.

Indeed, several genes related to ECM were differentially expressed in DCM and ICM FB, supporting a transcriptional basis for distinct fibrosis patterns between these aetiologies (Additional file 1: Fig. S9a). Interestingly, rhythmic processes (rhythmic process, circadian regulation of gene expression and entrainment of circadian clock by photoperiod) were among top GO terms enriched in DCM (Fig. 8b). To account for a potential confounding effect of fibrosis, we modelled fibrosis as a covariate in the DCM vs ICM comparison (using pseudobulk data approach in DESeq2); enrichment of circadian genes (Fisher test; $p = 0.0104$) and several ECM-related differences remained after adjustment, supporting the robustness of these findings (Additional file 2: Table S13).

Motivated by the reported involvement of circadian clock in cardiac diseases, including DCM [70–72], we explored the expression of genes underlying these GO pathways. Involved downregulated genes in DCM included those responsible for circadian transcription (*NPAS2*, *ARNTL*), whereas upregulated genes included *CRY1*, *PER1*, *PER2* and *3,* which negatively feedback to inhibit the transcription of the aforementioned genes. The downregulation of *NPAS2* and *ARNTL* in DCM was also apparent in the comparison with NF and ICM-scar, supporting a specific role in DCM (Fig. 8c). Notably, time of collection of cardiac samples did not contribute to differences in expression of these genes, and all DCM samples showed such transcriptional alterations (Additional file 1: Fig. S9b). Not all cell types in our analysis, e.g. CM, showed the same disruption in expression pattern of these genes, suggesting a prominent effect on circadian rhythm in DCM FB (Additional file 1: Fig. S9c-d). Given that many clock genes act in transcriptional control, we next used correlation analysis to identify the genes transcriptionally affected by this machinery. *ARNTL* expression correlated positively with *NPAS2*, while *PER2* and *PER3* were correlated negatively (Fig. 8d and Additional file 2: Table S12). Notably, *NPAS2* expression strongly correlated with *COL5A3* expression, which was decreased in expression in DCM compared to NF, ICM and ICM-scar (Fig. 8e). Notably, *COL5A3* regulates the assembly of fibres composed of type I and type V collagens and shows circadian rhythmicity [73].

Together, our data thus identify the unique gene signatures between ICM and DCM FB which may underlie different patterns of interstitial fibrosis.

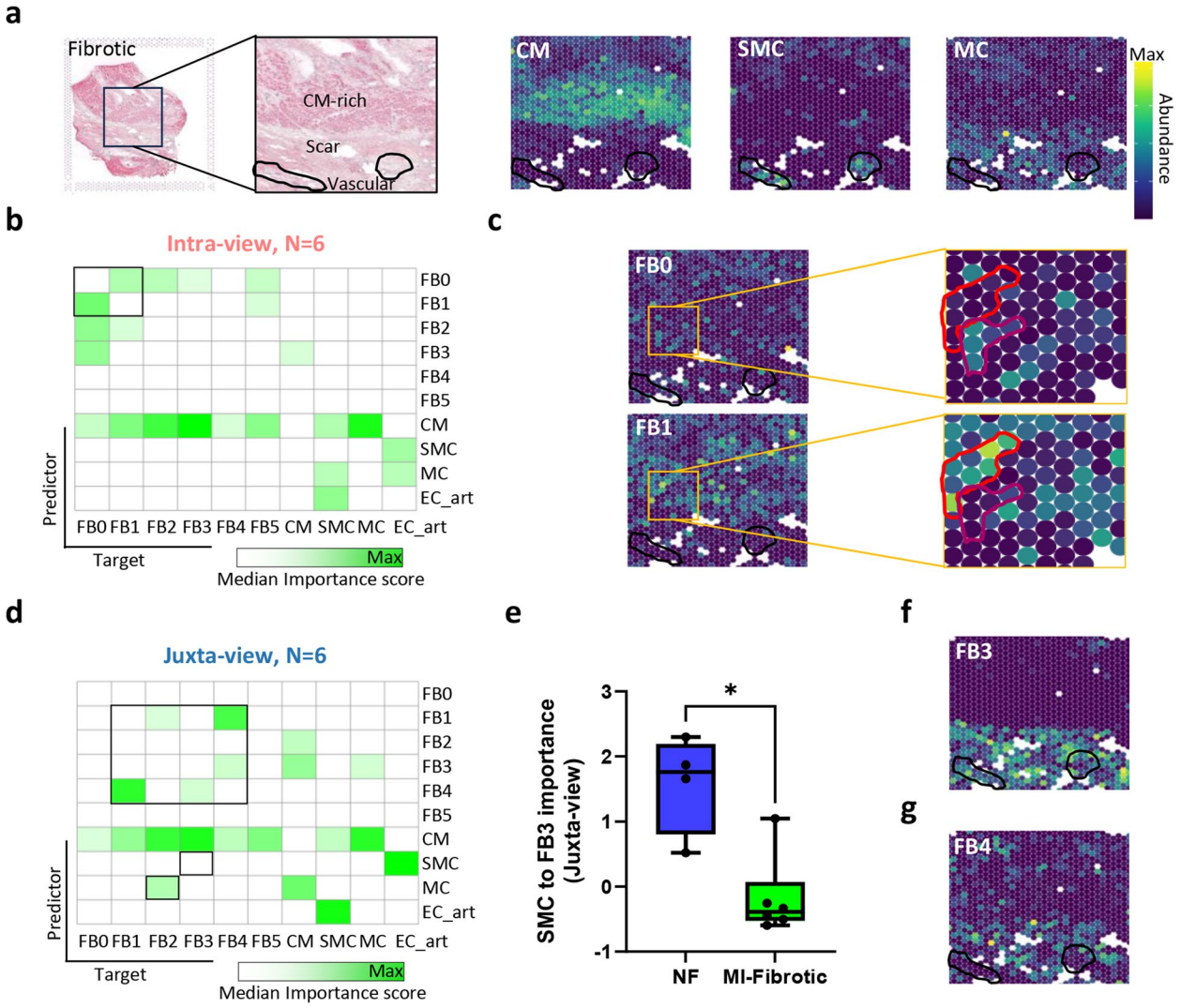

Fig. 6 Spatial distribution of FB states in the infarcted myocardium. **a** Left, Haematoxylin and eosin (H&E) staining of cardiac tissue after MI and visualization of a fibrotic region representative of samples used in the analysis (Fibrotic with mature scar). Sample ACH006. Right, Deconvoluted CM, MC, and SMC abundances in the same sample highlighting CM-rich region, scar region, and vascular areas. The indicated black area corresponds to the vasculature identified by H&E staining of the tissue. **b** Median importance of cell-type abundance (Predictors) in the prediction of abundances of other cell types (Targets) within a spot (Intra-view). White cells represent importance below the cut-off threshold (0.5). Green values indicate high importance scores which suggest within spot co-localisation or exclusion. **c** Left, Deconvoluted FB0 and FB1 abundances in the fibrotic sample showing abundance of FB0 and FB1 in CM-rich areas. Right, zoom in on 1 region with exclusivity of FB0 and FB1 within spots. Colours correspond to clusters; Bordeaux is an example of FB0 + spot, and red for FB1. **d** Median importance of cell-type abundance (Predictors) in the prediction of abundances of other cell types (Targets) in the immediate neighbouring tissue (Juxta-view). White cells represent importance below the cut-off threshold (0.5). Green value indicates high importance scores which suggest regional co-localisation or exclusion. **e** Importance scores showing dependency of FB3 on SMCs in the fibrotic regions according to the Juxta-view. The box shows the interquartile range with the median line; whiskers indicate min to max data. Two-sided Wilcoxon rank sum test. *, p value < 0.05. **f**-**i** Deconvoluted FB3,4,2, and 5 abundances in the fibrotic sample showing abundances of FB3 (**f**) and FB4 (**g**) in the scar region, FB2 (**h**) in perivascular areas, and FB5 (**i**) in the fibrotic region where CM-islands are present. CM; Cardiomyocytes, FB0, SMC; Smooth muscle cells, MC; Myeloid cells

Discussion

Fibrosis is a key determinant of deleterious cardiac remodelling during HF but is also key to cardiac repair post-MI [8, 32, 74]. Here, using RNA-seq of cardiac cell nuclei from NF and HF hearts of different aetiologies we gained new insights into the phenotypic changes and heterogeneity of FB remodelling in HF as well as the contribution of spatial cellular relationships therein. We identified unique trajectories of differentiation that coupled specific resting with differentiated states and the molecular cues that drive them. By comparing scar with non-scar FB, we identified exclusive previously unidentified states in the scar and unique features of FB in non-scar HF tissues.

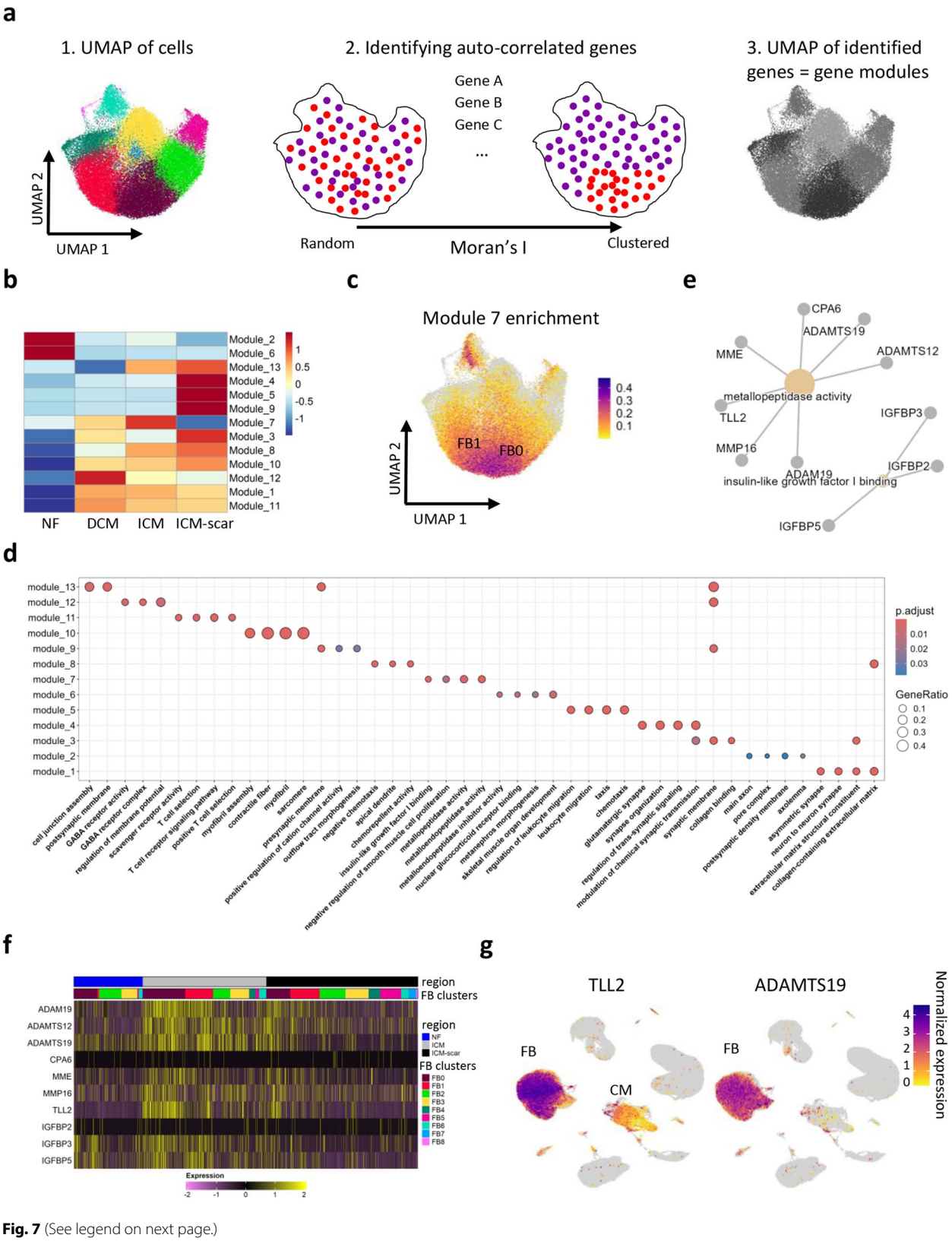

Fig. 7 (See legend on next page.)

(See figure on previous page.)

Fig. 7 Scar and interstitial fibrosis specific gene signatures in ICM. **a** Schematic showing the principle of gene module grouping. Moran's I statistic is calculated for each gene in the cells' UMAP. A positive value close to 1 indicates positive autocorrelation and suggests that close by cells have similar values of a certain gene's expression. Then, these genes are taken and grouped by a gene UMAP. **b** Heatmap showing the enrichment of different gene modules in HF and NF groups. **c** Feature plot showing the enrichment of Module 7 genes in FB0 and FB1. Enrichment was obtained by calculating a module score for Module 7 genes. **d** The top four enriched Gene Ontology pathways of each gene module. **e** Genes belonging to metallopeptidase activity and insulin like growth factor 1 (IGF1) binding (IGFBP) pathways. **f** Heatmap showing the expression of some module 7 genes (shown in e) across different FB states and different conditions. **g** Normalized expression level of TLL2 (left) and ADAMTS19 (right) in the snRNA-seq dataset showing specific expression in FB

Emergence of multiple activated FB states increases FB heterogeneity in HF

Consistent with previous studies, we identified FB together with CM and EC, as being the most abundant cell type in the heart [28, 29, 75]. While FB outnumbered EC in NF, they were less numerous in HF. This observation aligns with findings in [75], but not with that in [29]. The absence of an increase in FB proportion in these tissues likely reflects a stable fibrotic state that has developed during the extended time of progression to late-stage HF.

Of the cardiac cell types in our analysis, FB exhibited the greatest number of DEG across aetiologies, second only to CM. These data highlight the highly plastic nature of FB that allows them to adapt to different stresses and environments, and is consistent with the remodelling of FB to different functional states, with each specializing in different roles. Previous studies have identified between 4 and 7 FB states in NF heart and 4 and 13 in HF [16, 24, 26, 27, 29, 31, 44, 60]. Potentially owing to the diversity of samples analysed (NF,DCM, ICM both scar and non-scar) and the relatively high cell number and sequencing depth applied, we could detect 9 different cell states, including some at a low proportion (corresponding to a low cell number), with great certainty. Our study complements other studies and expand on them particularly in the area of FB biology, highlighting location and aetiology effects on FB activation.

The three resting FB populations (FB0, FB2, and FB3) that we identified have previously been classified as basal, oncostatin M receptor (OSMR)-expressing, and ECM-modulating states, respectively [26]. These three states were predominant in NF, accounting for over 80% of all FB but showed a significant reduction in HF. Consistently, FB2, which was also described as complement *C7* + *ABCA9* + FB state, was previously shown to decrease in ischaemic hearts [31]. FB3 resembled the *SCARA5* + *PCOLCE* + collagen processing FB [26, 29] and the MyoFB progenitor FB state reported to be capable of activation and collagen deposition after MI [31]. Further supporting this identification as resting states, FB0, and FB3 corresponded to respectively *COL15A1*$^{+}$, and *PI16*$^{+}$ FB states that were reported in a cross-tissue analysis of FB subpopulations to represent universal FB subtypes [44].

In HF, a large fraction of the FB population consists of the activated states, FB1 and FB4, which are low to absent in NF. Supporting a role in disease-associated fibrotic remodelling, these FB states expressed higher levels of fibrosis-related genes such as *POSTN* and *FAP*. FB1 was prominent across all HF samples, while FB4 was more enriched in DCM and ICM-scar tissue. The more elevated expression of fibrotic and ECM genes in FB4 suggested this state to be more activated than FB1. Elsewhere, FB1 and FB4 have been classified as a single activated/fibrotic/MyoFB state involved in TGF-β signalling owing to their similar expression of FB activation markers [26, 28, 31]. FB1 has also been shown to lie closer to a *TNC* + FB state [29] and FB4 to a *THBS4* + FB state [24] and to a state classified by its expression of *COMP (*identified in artery/tendon tissue*)* [44], indicating that it is closer to the previously described matrifibrocyte state [9].

FB5 showed a significant increase in DCM, and even greater in scar. This FB state resembled an *ELN* + differentiated FB state increased in DCM [29], but did not show substantial similarities with any other published FB states. FB5 exhibited some similarity to MyoFB but to a lesser extent than FB1/FB4 [31]. Whether FB5 is typical MyoFB or a de-differentiated phenotype remains to be studied. Two additional states were also identified in the scar, FB7 and 8, further increasing FB heterogeneity in this tissue. FB7 and FB8, appeared to be undescribed FB states, though FB7 showed some similarity to *SERPINE1* + and *CCL2* + FB and FB8 showed some similarity to *COMP* + FB [29, 44]. In common between these scar-enriched states is the presence of MyoFB characteristics and ECM remodelling capacity (e.g. ELN + in FB5), which may allow them to sustain the structural integrity of the scar.

Together, the data support that increased heterogeneity of FB states in HF contributes to heterogeneity of fibrous tissue within the failing heart, including more structured scar tissue. A summary of our cohort and FB states in relation to literature can be found in Additional file 2: Table S15.

Location determines pathways for FB activation

The evolution from 3 dominant states in NF to 6 in HF is consistent with a model in which the 3 resting FB states of NF, which persist at a lower level in HF, represent progenitors of the new states that emerge in HF. Previous reports have identified distinct cellular niches where FB become activated, suggesting a key role for specific

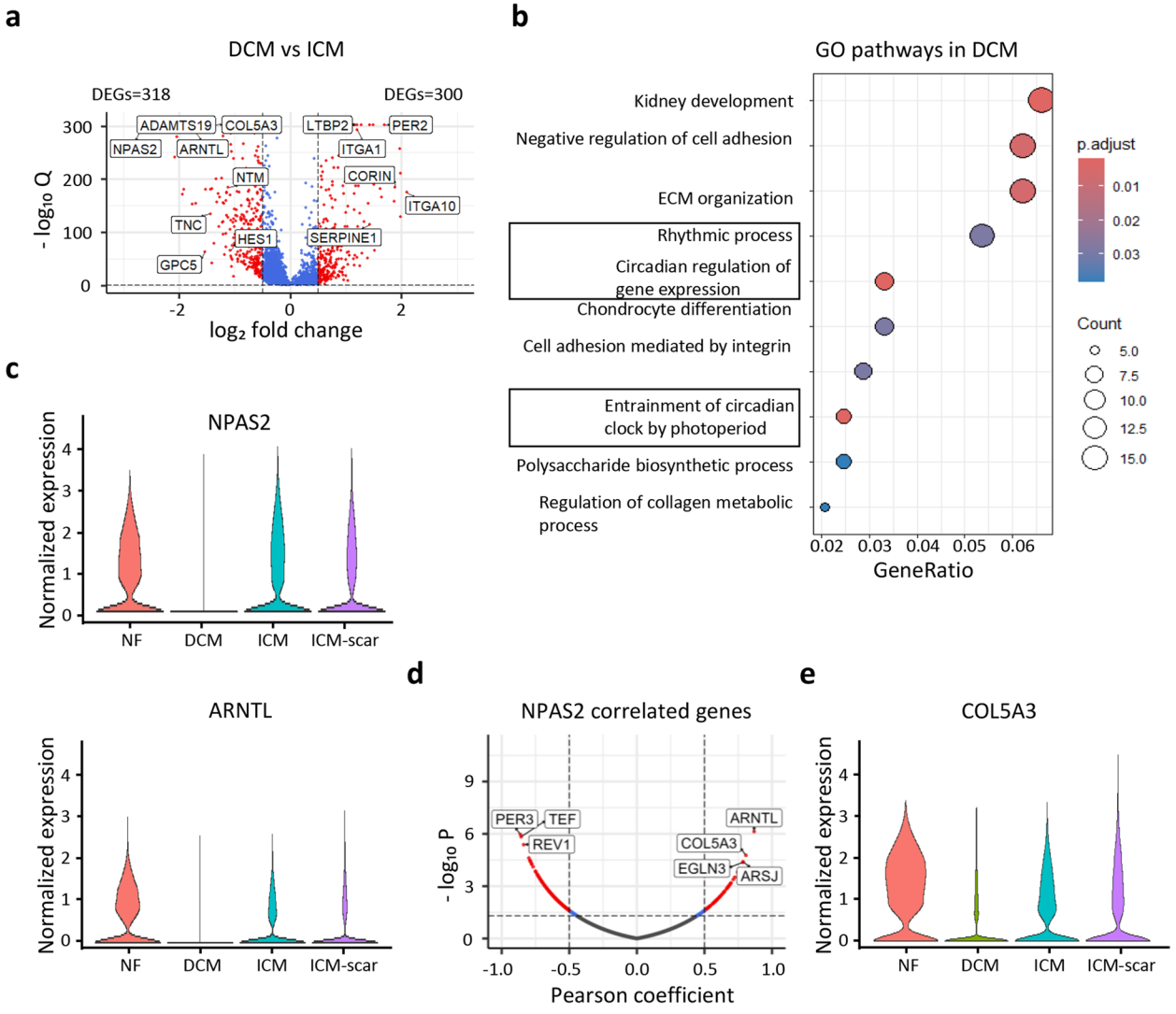

Fig. 8 Circadian rhythm disruption characterizes interstitial fibrosis in DCM. **a** Volcano plot showing ICM (left side) and DCM (right side) DEG. Some relevant genes are labelled. Q; adjusted p value. **b** The top 15 enriched Gene Ontology pathways of DCM FB DEGs compared to ICM FB. **c** Violin plots of normalized expression of NPAS2 (upper) and ARNTL (lower) in FB across different conditions. **d** Volcano plot representing positively (right) and negatively (left) correlated genes to NPAS2. The red colour represents the genes that have an absolute Pearson coefficient value > 0.5 and adjusted *p* value < 0.05. **e** Violin plot of normalized expression of COL5A3 in FB across different conditions

activating cues and signalling mechanisms in this process [16, 31]. Here our data provides new insights into signals that activate each of the resting states, linked to their location and that are related to cell–cell signalling.

As well as interaction with other cell types, suggesting a key role for FB in determining their own differentiation, they are preeminent amongst the ligand secreting cell types [76]. We similarly noted that in HF, FB showed increased cell–cell interactions including with themselves. Through combining this information of inferred cell–cell interactions with differentiation trajectories between states, and integration with spatial transcriptomics data sets, we could establish that the three resting states FB0, 2, and 3 represented progenitors for FB1, 5 and 4, respectively, and determined the main signals that contributed to their activation. Notably, each of the resident FB states showed differences in both expression and localization within the tissue, suggesting specialization of function. Indeed, our spatial mapping showed that FB3 predominantly resides in perivascular regions, whereas FB0 is mainly found within interstitial spaces. Consistently, ligands that contribute to activation of FB0, such as *JAM2*, are expressed in EC and CM and upregulated during HF. *PDGFB*, involved in FB2 activation, is expressed in myeloid cells and upregulated during HF, while *FGF1*, involved in FB3 activation, is primarily found in pericytes and smooth muscle cells (SMCs) and is upregulated during HF. This suggests distinct interactions between FB0 and CM, FB2 and immune cells, and FB3 and the vasculature.

Consistent with transition from interstitial FB0, activated FB1 was also localized in the CM-rich interstitium. FB4 on the other hand, invades fibrotic areas after perivascular FB3 transition. At these locations, FB became activated by a diverse array of ligands with some being unique to each resting FB state. FB5 was unlike other activated states. Specifically, FB5 which resembles a MyoFB state, and which is enriched in ICM-scar, is unlike activated FB1 and FB4 in terms of expression and trajectory of differentiation.

Together these data underscore the different spatial origin and multiple activation trajectories of FB in HF, resulting in a new spatial organization into interstitial fibrosis and scar fibrosis.

Interstitial fibrosis and scar have distinct FB states and signatures

Replacement scar is indispensable for maintaining LV structural integrity, and preventing cardiac rupture [32]. Hence, targeting reactive interstitial and perivascular fibrosis requires identification of targets that are not shared with scar tissue.

In scar, we found three gene modules enriched in collagen binding, ECM constituents, synapse organization, and leukocyte migration that were highly upregulated and not in non-scar, suggesting that this region supports a more stable ECM niche. Deriving gene modules in UMAP space has been debated and true metric relationships between nuclei in the UMAP embedding used for Moran's I may not correspond to their proximity in the original high-dimensional expression space [77]. While this is a limitation of the analysis marking the data as exploratory, a similar underlying biological signal was identified in an independent NMF-based analysis.

Importantly, non-scar tissue of ICM but also DCM, had increased expression of a gene module enriched for metallopeptidase activity and Insulin-like growth factor binding, which suggest a role in matrix degradation and instability. The insulin-like growth factor binding pathway comprised IGFBP2,3, and 5, and the metallopeptidase activity pathway involved *ADAM19*, *ADAMTS12*, *ADAMTS19*, *CPA6*, *MME*, *MMP16*, and *TLL2* (Fig. 7e). *IGFBP5* has been implicated in pulmonary fibrosis [78]. *MME*-encoded membrane metalloendopeptidase (also known as Neprilysin) is an endopeptidase responsible for degrading various vasoactive peptides. *TLL2* encodes tolloid-like 2 (TLL-2), a member of the BMP-1/TLD metalloprotease family. While TLL-2 is highly expressed during muscle development, its expression is minimal under normal physiological conditions adult [79, 80]. Unlike other BMP-1 family members, TLL-2 lacks procollagen C-proteinase activity but plays a role in extracellular matrix remodelling by processing pro-lysyl oxidase [63, 80], leading to its activation and subsequent collagen crosslinking. Additionally, TLL-2 activates myostatin by cleaving its latent complex, promoting muscle atrophy and fibrosis [81–83].

Together these data highlight unique features of interstitial and scar FB gene signatures.

Translational perspectives

Our data identify possible molecular targets to reduce reactive interstitial fibrosis without degrading structural scar, a challenge typically encountered in ICM, although the same targets would be useful in non-ICM pathology. First, we provided trajectories of activation and differentiation of resting FB, together with the main transcriptional regulators governing these transitions. The functional relevance of some of these transcriptional regulators, including *AEBP1* and *MEOX1* has been previously recognized. For example, *AEBP1* was shown to be increased in patients with persistent hypertrophy due to aortic stenosis and HF [84]. *MEOX1* was shown to be a key regulator of FB activation linked to cardiac dysfunction and to be increased in expression following the activation of fibroblasts in the human lung, liver, and kidney [85]. Second, the products of the unique gene expression patterns in non-scar are potential antifibrotic targets, consistent with clinical data. Neprilysin inhibition is incorporated into the latest HF treatment guidelines, particularly in combination with angiotensin receptor blockers (ARBs) like valsartan (ARNi therapy). This therapeutic approach has proven highly effective in reducing the risk of mortality and HF-related hospitalizations in patients with NYHA class II to III HF [86], and could be related to reduction of fibrosis. Notably, inclusion of sacubitril inhibition of neprilysin with valsartan in a mouse model of pressure overload significantly reduced interstitial fibrosis but had no impact on perivascular fibrosis, further reinforcing our findings [87].

Our analysis also identified the existence of DCM-specific FB features related to abnormal circadian rhythm. Disrupted circadian rhythms have been linked to the development of DCM in animal models [72]. A recent study also identified circadian rhythm abnormalities in DCM patients with sleep apnoea, which correlated with more severe left ventricular dilation and a higher incidence of arrhythmias [88]. However, abnormalities in circadian gene expression were not accompanied by increased histological fibrosis, suggesting that the circadian rhythm pathway contributes to the DCM phenotype independently of fibrosis. *COL5A3* was however correlated with circadian rhythm and downregulated in DCM. Whether this collagen isoform remodelling contributes to the decline in matrix tensile strength and the disrupted myocardial architecture observed in DCM deserves future investigation.

Conclusions

Our study identified the resting progenitor FB states and the activation pathways that result in the heterogeneity and spatial complexity of fibrosis in human end-stage HF. The persistence of unique gene expressions in interstitial fibrosis compared to scar indicates potential for targeted fibrosis therapies.

Abbreviations

snRNA-Seq	Single nucleus RNA sequencing
MI	Myocardial infarction
HF	Heart failure
NF	Non-failing
FB	Fibroblast
ICM	Ischemic cardiomyopathy
DCM	Dilated cardiomyopathy
MyoFB	Myofibroblasts
CM	Cardiomyocytes
EC	Endothelial cells
SMC	Smooth muscle cells
MC	Myeloid cells
KEGG	Kyoto encyclopedia of genes and genomes
GO	Gene ontology
DEG	Differentially expressed genes

Supplementary Information

The online version contains supplementary material available at https://doi.org/10.1186/s13073-025-01580-z.

Additional file 1: Supplementary figures, Fig. S1 (quality control and cellular identification), Fig. S1 (cardiac cellular distribution), Fig. S3 (correlation to histology), Fig. S4 (fibroblast states), Fig. S5 (comparison with literature), Fig. S6 (trajectory analysis), Fig. S7 (fibroblast activation and cellular communication), Fig. S8 (spatial transcriptomics), Fig. S9 (fibroblast states markers), Fig. S10 (circadian rhythm in DCM).

Additional file 2: This Excel file contains 16 worksheets: Supplementary tables description (legends), Table S1 (patient characteristics), Table S2 (cell types markers), Table S3 (average proportions of cell types), Table S4 (proportions of cardiac cell types per sample), Table S5 (correlation to fibrosis), Table S6 (fibroblast states markers), Table S7 (fibroblast states GO pathways), Table S8 (fibroblast states KEGG pathways), Table S9 (fibroblast specific genes correlated with fibrosis), Table S10 (Deconvolution evaluation composition), Table S11 (gene modules), Table S12 (ICM vs DCM genes, Wilcox test), Table S13 (ICM vs DCM genes, DESeq2+modelling fibrosis),Table S14 (genes correlated with NPAS2), Table S15 (summary comparison with literature).

Acknowledgements

We thank Roxane Menten for technical assistance. We thank the UZ Leuven Transplant Team the UZ Leuven Cardiac Surgery team for their support and assistance in tissue procurement. We acknowledge the KU Leuven Flow and Mass Cytometry core facility for cell sorting support. We thank the Saez-Rodríguez group for providing us with the gene-marker tables for fibroblast states described in [69] ahead of publication.

Authors' contributions

K.R.S., H.L.R., M.Y. designed experiments. M.Y., K.R.S., S.E-T., H.L.R. performed data curation and formal analysis. M.Y., R.D.P., C.K.N. performed experiments/acquired data. M.Y., K.R.S., H.L.R wrote the manuscript. F.R., M.Y., H.L.R. and K.R.S. contributed to Resources. S.E-T., B.T. contributed to methodology. All authors read and approved the final manuscript. K.R.S. and H.L.R. supervised the work.

Funding

This work was supported by project grants G0C7319N to KRS and FR, G0C6419N to HLR and G097021N to KRS and HLR from the FWO (Research Foundation Flanders) and by a C1 grant C14/21/093 to HLR and KRS from the research fund of KU Leuven. M.Y. received PhD stipend support from the Department of Cardiovascular Sciences, KU Leuven.

Data availability

The datasets generated and analysed during the current study are available in the Gene Expression Omnibus (GEO) repository, accession number [GSE298023](https://www.ncbi.nlm.nih.gov/geo/query/acc.cgi?acc=GSE298023) [89]. All source data are provided within the paper and its supplementary information files. Marker genes from other datasets used for comparison were obtained from the following studies [16, 26, 29, 31, 44, 60, 68, 69]. Spatial data were obtained from the study by [Kuppe et al.] (https://zenodo.org/records/6578047) [31, 90]. Atherosclerosis single-cell data were obtained from the study by [Wirka et al.] (https://static-content.springer.com/esm/art%3A10.1038%2Fs41591-019-0512-5/MediaObjects/41591_2019_512_MOESM1_ESM.xlsx) [45]. Histology images for corresponding fibroblast marker genes were obtained from the human protein atlas project [59]. The base analysis code is available at: (https://github.com/Rodericklab/FB-heterogeneity) [91].

Declarations

Ethics approval and consent to participate

The study protocol conformed to the Helsinki declaration, was conducted according to national and European Union regulations and was approved by the ethical committee of UZ Leuven (S58824). The study makes use of human tissues that are residual during standard care, which by law does not require prior informed consent. This also applies to the non-used donor tissues. Citizens can opt-out of donation or the use of their tissues for research at the time of death, which is recorded in national databases and checked at the time of donation. None of the included individuals had opted-out.

Consent for publication

Not applicable.

Competing interests

The authors declare no competing interests.

Author details

[1]Experimental Cardiology, Department of Cardiovascular Sciences, KU Leuven, Leuven 3000, Belgium
[3]Laboratory for Functional Epigenetics, Department of Genetics, KU Leuven, Leuven 3000, Belgium
[2]Cardiac Surgery, Department of Cardiovascular Sciences, KU Leuven, 3000 Leuven, Belgium
[4]Laboratory for Single Cell Omics (LISCO), KU Leuven, 3000 Leuven, Belgium
[5]Present address: Department of Immunology and Infection, Biomedical Research Institute, Hasselt University, 3590 Diepenbeek, Belgium

Received: 10 June 2025 / Accepted: 12 November 2025
Published online: 27 November 2025

References

1. Díez J, de Boer RA. Management of cardiac fibrosis is the largest unmet medical need in heart failure. Cardiovasc Res. 2022;118(2):e20-2.
2. Hara A, Tallquist MD. Is disrupting cardiac fibrosis a rational strategy for treating heart disease? Nat Cardiovasc Res. 2022;1(5):405–7.
3. Díez J, González A, López B, Querejeta R. Mechanisms of disease: pathologic structural remodeling is more than adaptive hypertrophy in hypertensive heart disease. Nat Clin Pract Cardiovasc Med. 2005;2(4):209–16.
4. Paulus WJ, Zile MR. From systemic inflammation to myocardial fibrosis. Circ Res. 2021;128(10):1451–67.
5. Brilla CG, Matsubara LS, Weber KT. Antifibrotic effects of spironolactone in preventing myocardial fibrosis in systemic arterial hypertension. Am J Cardiol. 1993;71(3):A12-6.
6. Deswal A, Richardson P, Bozkurt B, Mann DL. Results of the randomized aldosterone antagonism in heart failure with preserved ejection fraction trial (RAAM-PEF). J Card Fail. 2011;17(8):634–42.

7. McDiarmid AK, Swoboda PP, Erhayiem B, Bounford KA, Bijsterveld P, Tyndall K, et al. Myocardial effects of aldosterone antagonism in heart failure with preserved ejection fraction. J Am Heart Assoc. 2020;9(1):e011521.
8. Sweeney M, Corden B, Cook SA. Targeting cardiac fibrosis in heart failure with preserved ejection fraction: mirage or miracle? EMBO Mol Med. 2020;12(10):e10865.
9. Fu X, Khalil H, Kanisicak O, Boyer JG, Vagnozzi RJ, Maliken BD, et al. Specialized fibroblast differentiated states underlie scar formation in the infarcted mouse heart. J Clin Invest. 2018;128(5):2127–43.
10. Galindo CL, Kasasbeh E, Murphy A, Ryzhov S, Lenihan S, Ahmad FA, et al. <article-title update="added">Anti-Remodeling and Anti-Fibrotic Effects of the Neuregulin-1β Glial Growth Factor 2 in a Large Animal Model of Heart Failure. J Am Heart Assoc. 2014;3(5):e000773.
11. Nagaraju CK, Robinson EL, Abdesselem M, Trenson S, Dries E, Gilbert G, et al. Myofibroblast phenotype and reversibility of fibrosis in patients with end-stage heart failure. J Am Coll Cardiol. 2019;73(18):2267–82.
12. Wang H, Haeger SM, Kloxin AM, Leinwand LA, Anseth KS. Redirecting valvular myofibroblasts into dormant fibroblasts through light-mediated reduction in substrate modulus. PLoS One. 2012;7(7):e39969.
13. Lewis GA, Dodd S, Clayton D, Bedson E, Eccleson H, Schelbert EB, et al. Pirfenidone in heart failure with preserved ejection fraction: a randomized phase 2 trial. Nat Med. 2021;27(8):1477–82.
14. Humeres C, Frangogiannis NG. Fibroblasts in the Infarcted, Remodeling, and Failing Heart. JACC: Basic to Translational Science. 2019;4(3):449–67.
15. Alexanian M, Padmanabhan A, Nishino T, Travers JG, Ye L, Pelonero A, et al. Chromatin remodelling drives immune cell–fibroblast communication in heart failure. Nature. 2024;635(8038):434–43.
16. Amrute JM, Luo X, Penna V, Yang S, Yamawaki T, Hayat S, et al. Targeting immune–fibroblast cell communication in heart failure. Nature. 2024;635(8038):423–33.
17. Aghajanian H, Kimura T, Rurik JG, Hancock AS, Leibowitz MS, Li L, et al. Targeting cardiac fibrosis with engineered T cells. Nature. 2019;573(7774):430–3.
18. Wang J, Du H, Xie W, Bi J, Zhang H, Liu X, et al. CAR-macrophage therapy alleviates myocardial ischemia-reperfusion injury. Circ Res. 2024;135(12):1161–74.
19. Takeda N, Manabe I, Uchino Y, Eguchi K, Matsumoto S, Nishimura S, et al. Cardiac fibroblasts are essential for the adaptive response of the murine heart to pressure overload. J Clin Invest. 2010;120(1):254–65.
20. Kanisicak O, Khalil H, Ivey MJ, Karch J, Maliken BD, Correll RN, et al. Genetic lineage tracing defines myofibroblast origin and function in the injured heart. Nat Commun. 2016;7(1):12260.
21. Ali SR, Ranjbarvaziri S, Talkhabi M, Zhao P, Subat A, Hojjat A, et al. Developmental heterogeneity of cardiac fibroblasts does not predict pathological proliferation and activation. Circ Res. 2014;115(7):625–35.
22. Moore-Morris T, Guimarães-Camboa N, Banerjee I, Zambon AC, Kisseleva T, Velayoudon A, et al. Resident fibroblast lineages mediate pressure overload–induced cardiac fibrosis. J Clin Invest. 2014;124(7):2921–34.
23. Gladka MM, Molenaar B, de Ruiter H, van der Elst S, Tsui H, Versteeg D, et al. Single-cell sequencing of the healthy and diseased heart reveals cytoskeleton-associated protein 4 as a new modulator of fibroblasts activation. Circulation. 2018;138(2):166–80.
24. McLellan MA, Skelly DA, Dona MSI, Squiers GT, Farrugia GE, Gaynor TL, et al. High-resolution transcriptomic profiling of the heart during chronic stress reveals cellular drivers of cardiac fibrosis and hypertrophy. Circulation. 2020;142(15):1448–63.
25. Palmer JA, Rosenthal N, Teichmann SA, Litvinukova M. Revisiting cardiac biology in the era of single cell and spatial omics. Circ Res. 2024;134(12):1681–702.
26. Litviňuková M, Talavera-López C, Maatz H, Reichart D, Worth CL, Lindberg EL, et al. Cells of the adult human heart. Nature. 2020;588(7838):466–72.
27. Tucker NR, Chaffin M, Fleming SJ, Hall AW, Parsons VA, Bedi KC, et al. Transcriptional and cellular diversity of the human heart. Circulation. 2020;142(5):466–82.
28. Chaffin M, Papangeli I, Simonson B, Akkad AD, Hill MC, Arduini A, et al. Single-nucleus profiling of human dilated and hypertrophic cardiomyopathy. Nature. 2022;608(7921):174–80.
29. Koenig AL, Shchukina I, Amrute J, Andhey PS, Zaitsev K, Lai L, et al. Single-cell transcriptomics reveals cell-type-specific diversification in human heart failure. Nat Cardiovasc Res. 2022;1(3):263–80.
30. Wang L, Yu P, Zhou B, Song J, Li Z, Zhang M, et al. Single-cell reconstruction of the adult human heart during heart failure and recovery reveals the cellular landscape underlying cardiac function. Nat Cell Biol. 2020;22(1):108–19.
31. Kuppe C, Ramirez Flores RO, Li Z, Hayat S, Levinson RT, Liao X, et al. Spatial multi-omic map of human myocardial infarction. Nature. 2022;608(7924):766–77.
32. Frangogiannis NG. Cardiac fibrosis. Cardiovasc Res. 2021;117(6):1450–88.
33. Hilgendorf I, Frantz S, Frangogiannis NG. Repair of the infarcted heart: cellular effectors, molecular mechanisms and therapeutic opportunities. Circ Res. 2024;134(12):1718–51.
34. Amoni M, Vermoortele D, Ekhteraei-Tousi S, Doñate Puertas R, Gilbert G, Youness M, et al. Heterogeneity of repolarization and cell-cell variability of cardiomyocyte remodeling within the myocardial infarction border zone contribute to arrhythmia susceptibility. Circ Arrhythm Electrophysiol. 2023;16(5):e011677.
35. Thienpont B, Aronsen JM, Robinson EL, Okkenhaug H, Loche E, Ferrini A, et al. The H3K9 dimethyltransferases EHMT1/2 protect against pathological cardiac hypertrophy. J Clin Invest. 2016;127(1):335–48.
36. Preissl S, Schwaderer M, Raulf A, Hesse M, Grüning BA, Köbele C, et al. Deciphering the epigenetic code of cardiac myocyte transcription. Circ Res. 2015;117(5):413–23.
37. Fleming SJ, Chaffin MD, Arduini A, Akkad AD, Banks E, Marioni JC, et al. Unsupervised removal of systematic background noise from droplet-based single-cell experiments using cell bender. Nat Methods. 2023;20(9):1323–35.
38. Nassiri I, Kwok AJ, Bhandari A, Bull KR, Garner LC, Klenerman P, et al. Demultiplexing of single-cell RNA-sequencing data using interindividual variation in gene expression. Bioinformatics Adv. 2024;4(1):vbae05.
39. Germain PL, Lun A, Garcia Meixide C, Macnair W, Robinson MD. Doublet identification in single-cell sequencing data using scDblFinder. F1000Res. 2021;10:979.
40. Hao Y, Hao S, Andersen-Nissen E, Mauck WM, Zheng S, Butler A, et al. Integrated analysis of multimodal single-cell data. Cell. 2021;184(13):3573-3587.e29.
41. Korsunsky I, Millard N, Fan J, Slowikowski K, Zhang F, Wei K, et al. Fast, sensitive and accurate integration of single-cell data with Harmony. Nat Methods. 2019;16(12):1289–96.
42. Hocker JD, Poirion OB, Zhu F, Buchanan J, Zhang K, Chiou J, et al. Cardiac cell type–specific gene regulatory programs and disease risk association. Sci Adv. 2021;7(20):eabf1444.
43. Zappia L, Oshlack A. Clustering trees: a visualization for evaluating clusterings at multiple resolutions. Gigascience. 2018;7(7):giy083.
44. Buechler MB, Pradhan RN, Krishnamurty AT, Cox C, Calviello AK, Wang AW, et al. Cross-tissue organization of the fibroblast lineage. Nature. 2021;593(7860):575–9.
45. Wirka RC, Wagh D, Paik DT, Pjanic M, Nguyen T, Miller CL, et al. Atheroprotective roles of smooth muscle cell phenotypic modulation and the TCF21 disease gene as revealed by single-cell analysis. Nat Med. 2019;25(8):1280–9.
46. Phipson B, Sim CB, Porrello ER, Hewitt AW, Powell J, Oshlack A. Propeller: testing for differences in cell type proportions in single cell data. Bioinformatics. 2022;38(20):4720–6.
47. Saul D, Kosinsky RL, Atkinson EJ, Doolittle ML, Zhang X, LeBrasseur NK, et al. A new gene set identifies senescent cells and predicts senescence-associated pathways across tissues. Nat Commun. 2022;13(1):4827.
48. Love MI, Huber W, Anders S. Moderated estimation of fold change and dispersion for RNA-seq data with DESeq2. Genome Biol. 2014;15(12):550.
49. Naba A, Clauser KR, Hoersch S, Liu H, Carr SA, Hynes RO. The matrisome: in silico definition and in vivo characterization by proteomics of normal and tumor extracellular matrices*. Mol Cell Proteomics. 2012;11(4):M111.014647.
50. Conway JR, Lex A, Gehlenborg N. UpsetR: an R package for the visualization of intersecting sets and their properties. Bioinformatics. 2017;33(18):2938–40.
51. Yu G, Wang LG, Han Y, He QY. Clusterprofiler: an R package for comparing biological themes among gene clusters. OMICS. 2012;16(5):284–7.
52. Trapnell C, Cacchiarelli D, Grimsby J, Pokharel P, Li S, Morse M, et al. The dynamics and regulators of cell fate decisions are revealed by pseudotemporal ordering of single cells. Nat Biotechnol. 2014;32(4):381–6.
53. Yerly L, Andreatta M, Garnica J, Nardin C, Domizio JD, Aubin F, et al. Wounding triggers invasive progression in human basal cell carcinoma. bioRxiv 2024.05.31.596823; https://doi.org/10.1101/2024.05.31.596823.
54. Street K, Risso D, Fletcher RB, Das D, Ngai J, Yosef N, et al. Slingshot: cell lineage and pseudotime inference for single-cell transcriptomics. BMC Genomics. 2018;19(1):477.
55. Van den Berge K, de Roux Bézieux H, Street K, Saelens W, Cannoodt R, Saeys Y, et al. Trajectory-based differential expression analysis for single-cell sequencing data. Nat Commun. 2020;11(1):1201.

56. Lambert SA, Jolma A, Campitelli LF, Das PK, Yin Y, Albu M, et al. The human transcription factors. Cell. 2018;172(4):650–65.
57. Browaeys R, Saelens W, Saeys Y. Nichenet: modeling intercellular communication by linking ligands to target genes. Nat Methods. 2020;17(2):159–62.
58. Rahimi A, Vale-Silva LA, Fälth Savitski M, Tanevski J, Saez-Rodriguez J. DOT: a flexible multi-objective optimization framework for transferring features across single-cell and spatial omics. Nat Commun. 2024;15(1):4994.
59. Uhlén M, Fagerberg L, Hallström BM, Lindskog C, Oksvold P, Mardinoglu A, et al. Tissue-based map of the human proteome. Science. 2015;347(6220):1260419.
60. Rao M, Wang X, Guo G, Wang L, Chen S, Yin P, et al. Resolving the intertwining of inflammation and fibrosis in human heart failure at single-cell level. Basic Res Cardiol. 2021;116(1):55.
61. Imanaka-Yoshida K, Hiroe M, Nishikawa T, Ishiyama S, Shimojo T, Ohta Y, et al. Tenascin-C modulates adhesion of cardiomyocytes to extracellular matrix during tissue remodeling after myocardial infarction. Lab Invest. 2001;81(7):1015–24.
62. Imanaka-Yoshida K, Tawara I, Yoshida T. Tenascin-C in cardiac disease: a sophisticated controller of inflammation, repair, and fibrosis. Am J Physiol Cell Physiol. 2020;319(5):C781-96.
63. Uzel MI, Scott IC, Babakhanlou-Chase H, Palamakumbura AH, Pappano WN, Hong HH, et al. Multiple bone morphogenetic protein 1-related mammalian metalloproteinases process pro-lysyl oxidase at the correct physiological site and control lysyl oxidase activation in mouse embryo fibroblast cultures. J Biol Chem. 2001;276(25):22537–43.
64. Ghosh AK, Rai R, Flevaris P, Vaughan DE. Epigenetics in reactive and reparative cardiac fibrogenesis: the promise of epigenetic therapy. J Cell Physiol. 2017;232(8):1941–56.
65. Ton QV, Leino D, Mowery SA, Bredemeier NO, Lafontant PJ, Lubert A, et al. Collagen COL22A1 maintains vascular stability and mutations in COL22A1 are potentially associated with intracranial aneurysms. Dis Model Mech. 2018;11(12):dmm033654.
66. van Nieuwenhoven FA, Munts C, Op't Veld RC, González A, Díez J, Heymans S, et al. Cartilage intermediate layer protein 1 (CILP1): a novel mediator of cardiac extracellular matrix remodelling. Sci Rep. 2017;7(1):16042.
67. Watanabe T, Baker Frost D, Mlakar L, Heywood J, da Silveira WA, Hardiman G, et al. A human skin model recapitulates systemic sclerosis dermal fibrosis and identifies COL22A1 as a TGFβ early response gene that mediates fibroblast to myofibroblast transition. Genes. 2019;10(2):75.
68. Reichart D, Lindberg EL, Maatz H, Miranda AMA, Viveiros A, Shvetsov N, et al. Pathogenic variants damage cell composition and single cell transcription in cardiomyopathies. Science. 2022;377(6606):eabo1984.
69. Lanzer JD, Ramirez Flores RO, Liñares Blanco J, Steier M, Rangrez AY, Frey N, et al. A cross-study transcriptional patient map of heart failure defines conserved multicellular coordination in cardiac remodeling. Nat Commun. 2025;16(1):9659.
70. Rabinovich-Nikitin I, Lieberman B, Martino TA, Kirshenbaum LA. Circadian-regulated cell death in cardiovascular diseases. Circulation. 2019;139(7):965–80.
71. Lefta M, Campbell KS, Feng HZ, Jin JP, Esser KA. Development of dilated cardiomyopathy in Bmal1-deficient mice. Am J Physiol-Heart Circ Physiol. 2012;303(4):H475-85.
72. Song S, Tien CL, Cui H, Basil P, Zhu N, Gong Y, et al. Myocardial rev-erb–mediated diurnal metabolic rhythm and obesity paradox. Circulation. 2022;145(6):448–64.
73. Bennardo M, Alibhai F, Tsimakouridze E, Chinnappareddy N, Podobed P, Reitz C, et al. Day-night dependence of gene expression and inflammatory responses in the remodeling murine heart post-myocardial infarction. Am J Physiol-Regul Integr Comp Physiol. 2016;311(6):R1243–54.
74. Oka T, Xu J, Kaiser RA, Melendez J, Hambleton M, Sargent MA, et al. Genetic manipulation of periostin expression reveals a role in cardiac hypertrophy and ventricular remodeling. Circ Res. 2007;101(3):313–21.
75. Simonson B, Chaffin M, Hill MC, Atwa O, Guedira Y, Bhasin H, et al. Single-nucleus RNA sequencing in ischemic cardiomyopathy reveals common transcriptional profile underlying end-stage heart failure. Cell Rep. 2023;42(2):112086.
76. Farbehi N, Patrick R, Dorison A, Xaymardan M, Janbandhu V, Wystub-Lis K, et al. Single-cell expression profiling reveals dynamic flux of cardiac stromal, vascular and immune cells in health and injury. eLife. 2019;8:e43882.
77. Chari T, Pachter L. The specious art of single-cell genomics. PLoS Comput Biol. 2023;19(8):e1011288.
78. Nguyen XX, Muhammad L, Nietert PJ, Feghali-Bostwick C. IGFBP-5 promotes fibrosis via increasing its own expression and that of other pro-fibrotic mediators. Front Endocrinol. 2018;15(9):601.
79. Allen DL, Greyback BJ, Hanson AM, Cleary AS, Lindsay SF. Skeletal muscle expression of bone morphogenetic protein-1 and tolloid-like-1 extracellular proteases in different fiber types and in response to unloading, food deprivation and differentiation. J Physiol Sci. 2010;60(5):343–52.
80. Scott IC, Blitz IL, Pappano WN, Imamura Y, Clark TG, Steiglitz BM, et al. Mammalian BMP-1/Tolloid-related metalloproteinases, including novel family member mammalian tolloid-like 2, have differential enzymatic activities and distributions of expression relevant to patterning and skeletogenesis. Dev Biol. 1999;213(2):283–300.
81. Knapp M, Supruniuk E, Górski J. Myostatin and the Heart Biomolecules. 2023;13(12):1777.
82. Lee SJ. Genetic analysis of the role of proteolysis in the activation of latent myostatin. PLoS One. 2008;3(2):e1628.
83. Wolfman NM, McPherron AC, Pappano WN, Davies MV, Song K, Tomkinson KN, et al. Activation of latent myostatin by the BMP-1/tolloid family of metalloproteinases. Proc Natl Acad Sci. 2003;100(26):15842–6.
84. Kattih B, Boeckling F, Shumliakivska M, Tombor L, Rasper T, Schmitz K, et al. Single-nuclear transcriptome profiling identifies persistent fibroblast activation in hypertrophic and failing human hearts of patients with longstanding disease. Cardiovasc Res. 2023;119(15):2550–62.
85. Alexanian M, Przytycki PF, Micheletti R, Padmanabhan A, Ye L, Travers JG, et al. A transcriptional switch governs fibroblast activation in heart disease. Nature. 2021;595(7867):438–43.
86. Bozkurt B, Nair AP, Misra A, Scott CZ, Mahar JH, Fedson S. Neprilysin inhibitors in heart failure. JACC: Basic to Translational Science. 2023;8(1):88–105.
87. Burke RM, Lighthouse JK, Mickelsen DM, Small EM. Sacubitril/valsartan decreases cardiac fibrosis in left ventricle pressure overload by restoring PKG signaling in cardiac fibroblasts. Circ Heart Fail. 2019;12(4):e005565.
88. Jia H, Cui H, Zhao Z, Mo H, Zhang N, Zhang Y, et al. Abnormal circadian rhythms exacerbate dilated cardiomyopathy by reducing the ventricular mechanical strength. Cardiovasc Res. 2024;120(17):2261–77.
89. Youness M, Ekhteraei-Tousi S, Doñate Puertas R, Nagaraju CK, Sipido KR, Roderick HL. Location and etiology modulate fibroblast activation in the failing human heart. NCBI Gene Expression Omnibus (GEO). 2025. https://www.ncbi.nlm.nih.gov/geo/query/acc.cgi?acc=GSE298023.
90. Kuppe C, Flores ROR, Li Z, Hayat S, Levinson RT, Liao X, et al. Processed Data 1 : Spatial multi-omic map of human myocardial infarction. Zenodo. 2022. https://zenodo.org/records/6578047.
91. Youness M. FB-heterogeneity. Github. 2025. https://github.com/Rodericklab/FB-heterogeneity.

Publisher's note